Engineering Fracture Mechanics 282 (2023) 109169

Contents lists available at ScienceDirect

Engineering Fracture Mechanics

journal homepage: www.elsevier.com/locate/engfracmech

Implementation and parametric study of J-integral data reduction methods for the translaminar toughness of hierarchical thin-ply composites

Guillaume Broggi [a,*], Joël Cugnoni [b], Véronique Michaud [a]

[a] Laboratory for Processing of Advanced Composites (LPAC), Institute of Materials (IMX), École Polytechnique Fédérale de Lausanne (EPFL), Station 12, 1015, Lausanne, Switzerland

[b] School of Management and Engineering Vaud, University of Applied Sciences and Arts Western (HES-SO), 1401, Yverdon-les-Bains, Switzerland

ARTICLE INFO

Keywords:
J-integral
Digital image correlation
Translaminar toughness
Thin-ply
Hybrid composites

ABSTRACT

Three different J-integral formulations to derive the experimental translaminar toughness of composites from compact tension tests with a large-scale fracture process zone are implemented and discussed. They improve the existing approaches by taking advantage of stereo-digital image correlation to acquire full-field displacement fields. A field fitting procedure based on robust and efficient piecewise cubic smooth splines addresses noise-related issues reported in previous studies. Additionally, the paper proposes a novel crack tip extraction procedure to report the energy release rate as a function of the crack increment, even if knowledge of the crack tip is not required for the proposed J-integral method. The three methods are discussed in light of a parametric study conducted on synthetic and experimental data, including artificially noisy data. The study reveals that the proposed J-integral methods are suitable for translaminar toughness evaluation of a wide range of materials without the need for restrictive assumptions. However, variations in propagation values were observed when applied to experimental data. Finally, guidelines are drawn to chose the most suitable parameters for the algorithms that are proposed as a Python package.

1. Introduction

The damage-tolerant design paradigm is a well-established and widely adopted approach to develop highly optimized composite parts and tailored laminate layups, to ensure the operational safety of critical load-bearing structures such as airframes [1]. The notion of damage encompasses a wide range of flaws that may appear prior to the part service life, such as manufacturing defects, or during use, such as fatigue and impact damage.

Thin-ply composites [2] have been shown to be remarkably tolerant to use-induced damage, among other benefits. Sihn et al. [3] and Amacher et al. [4] reported that thin-ply laminates do not suffer from fatigue under significant cyclic stress. Likewise, thin-ply FRPs retain superior load-carrying capacity after an impact [2,5,6]. These outstanding properties are explained by the in-situ effect [7–9], which delays or even suppresses micro-cracking, transverse cracking, and delamination in thin-ply laminates. Nevertheless, these mechanisms are dissipative and required to initiate secondary damage, such as crack splitting. Consequently, thin-ply composites exhibit a low translaminar toughness compared to regular FRPs. As a result, they are not tolerant to stress concentrators and are prone to quasi-brittle failure [4,10–13].

* Corresponding author.
E-mail addresses: guillaume.broggi@epfl.ch (G. Broggi), joel.cugnoni@heig-vd.ch (J. Cugnoni), veronique.michaud@epfl.ch (V. Michaud).

https://doi.org/10.1016/j.engfracmech.2023.109169
Received 23 November 2022; Received in revised form 19 February 2023; Accepted 25 February 2023
Available online 9 March 2023

Nomenclature

Δa	Crack increment
δ	Crack opening displacement (COD)
Δ_{AB}, Δ_{BC}, Δ_{CD}, Δ_{DE}, Δ_{EF}	Contour offset used to define the J-integral contour with respect to the crack tip
δ_{ij}	Kronecker delta
$\varnothing_a$	Crack tip diameter
Γ	Enclosing contour on which the line and simplified J-integral are evaluated
ν	Laminate Poisson ratio
σ	Stress tensor
ε	Strain tensor
A	Area of the enclosing contour on which the surface J-integral is evaluated
a	Crack length
a_0	Initial crack length
C	Laminate compliance tensor
dA	Infinitesimal surface
ds	Infinitesimal arc length along Γ
E	Laminate Young modulus
G	Laminate shear modulus
G_{Ic}	Mode I linear critical ERR
J	J-integral
J_{Ic}	Mode I critical nonlinear ERR
l_{FPZ}	Length of the FPZ
n	Outward unit normal vector along Γ
q	Smooth unit translation function
u	Displacement field
w	Strain density energy

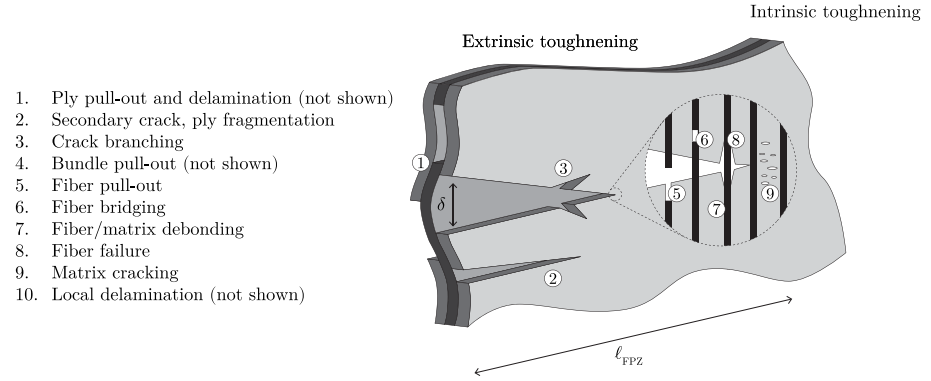

Fig. 1. Typical multi-scale damage modes in thick-ply or hierarchical thin-ply composites. The FPZ usually extends over several millimeters. *Source:* Adapted from [14,21].

Overall, the translaminar crack growth in materials involves extrinsic and intrinsic dissipative mechanisms [14]. These mechanisms act over a fracture process zone (FPZ) and are usually accounted for through the critical energy release rate (ERR). In thick-plies composites, these mechanisms typically include delamination, extensive fiber pull-out or fiber bridging (see Fig. 1) and affect a large FPZ, but these are precisely reduced or even suppressed in thin-ply laminates. Significant efforts have been made to restore these crack-shielding mechanisms in thin-ply laminates by engineering hierarchical microstructures, often following bio-inspired approaches [15–20]. Consequently, these hierarchical thin-ply composites exhibit non-linear and large-scale FPZ.

Compact tension (CT) is the prevailing test to grow stable cracks in composites and characterize their translaminar toughness [22], although different geometries have been recently proposed to overcome its limitations [19,23]. However, there is no standard data reduction methodology associated with CT samples to obtain the ERR. The most established ones rely on the linear elastic fracture mechanics (LEFM) theoretical framework to yield the mode I critical ERR G_{Ic} as a function of the crack increment Δa, commonly referred to as R-curve [24]. Most of these methods are challenging to apply to hierarchical thin-plies. Methods based on

the stress intensity factor were found to be inaccurate for orthotropic materials [24,25]. The compliance calibration methods were shown to be more adapted to composites but raise specific issues whether the compliance is derived from a closed-form formulated for orthotropic materials [26], an experimental fitting, or a FEM [25,27]. The first requires a negligible FPZ. The second offers the benefit of accounting for the FPZ but is unreliable since thin-ply composites tend to follow a saw-tooth behavior [13], meaning that too few propagation points are available for a robust fitting. Alternatively, the compliance may be fitted from specimens with an increasing machined crack length [24,28], but this consumes too much material and does not allow for capturing the effect of the FPZ in the wake of the crack, for instance, when extensive fiber pull-out occurs. Additionally, the experimental compliance fitting requires the crack length measurement. With a large FPZ the crack tip position is clearly ambiguous and subjective. Moreover, the crack tends to propagate differently in the bulk [29] and optical observation of the sample surface is usually not representative of the crack front. In-situ X-ray tomography has been successfully used to characterize the translaminar toughness [30] but this approach is cumbersome. The last approach, the modified compliance calibration (MCC), is based on FEM and does not require measuring the crack length. The MCC has recently been extensively used [11,12,16,31] but adds the overhead of a numerical model. It involves the a priori knowledge of material properties, damage mechanisms, and constitutive laws. Moreover, such a model does not account for the FPZ in the wake of the crack unless a cohesive law is specifically developed.

Furthermore, all these methods were derived under LEFM assumptions, even if not explicitly, see, for instance, the derivation of the Irwin–Kies equation [21]. Their validity is thus questionable in CT specimens exhibiting a large FPZ length l_{FPZ}. Ortega et al. [32] and Maimíet al. [33] have shown analytically and experimentally that R-curves obtained from LEFM-based methods are not independent of the sample size. When the length l_{FPZ} increases, such as in the presence of extensive pull-out, LEFM-based methods tend to overpredict the translaminar toughness. The later publication also reported that over-height compact tension (OCT) specimens [34,35] improve the ratio of l_{FPZ} to specimen size and thus better approximate LEFM conditions. However, this geometry requires large quantities of material and is not guaranteed to be large enough to develop a self-similar FPZ as reported by Xu et al. [36,37].

When the material response is non-linear, it is commonly admitted that the non-linear J-curve is an appropriate descriptor of the fracture process where crack stability is defined as $J_I < J_{Ic}$. The J-curve is more general than LEFM-based methods, accounts for material non-linearities such as plasticity as well as large FPZ, and has been shown to better account for the translaminar fracture toughness of composites [33]. When LEFM conditions are fulfilled, J_c is, therefore, equal to G_c as experimentally verified by several authors [31,38]. The J-curve has been derived by indirect and direct methods [39]. The former, also known as inverse methods, rely on the identification of the suitable parameters through an optimization procedure to match a FEM response with respect to experimental data, as used, for instance, by Frossard to identify bridging traction [40]. Regarding the translaminar toughness in CT specimens, Ortega et al. [41,42] proposed a cohesive law identification based on a generalized Dugdale–Barenblatt model. Based on J-integral approaches [43,44], the latter can be simplified to straightforward equations for selected geometries [45]. For the remaining geometries, including the CT specimen, the J-integral requires a numerical evaluation along a contour using full-field displacement data acquired, for instance, by digital image correlation (DIC) [13,31,46,47]. This experimental step is often criticized as cumbersome and subjected to scattering, leading to the preference for different methods. Nevertheless, J-integral methods are of great interest as they rely on conservative assumptions, i.e., material homogeneity and the knowledge of stress and strain over the evaluated contour, regardless of the constitutive equations used to derive them. They are, therefore, suitable for a wide range of geometries and materials, including hierarchical thin-ply or thick-ply laminates, as long the FPZ is included inside the J-integral contour.

One of the reasons behind the prevalence of the MCC compared to the J-integral to derive the translaminar toughness of composite CT specimens is probably the lack of published practical guidelines, reinforcing the notion that this approach is complex and challenging to master. Several publications reported using J-integral methods [31,38,48,49] but the details of the numerical derivation and its sensitivity to noise or parameter variations are rarely discussed. One of the best efforts in this regard is the JMAN routine proposed by Becker et al. [48] and reported as an efficient implementation of the surface J-integral. However, too few details are given about its implementation, i.e, the code was not distributed to the best of the authors' knowledge. Indeed, many solutions with different pitfalls may be implemented to derive the J-integral, which leads to costly development. Publication of the code is therefore deemed necessary to further diffuse the J-integral method. More recently, Barhli et al. [49] made available the Oxford University Reinjection-Optimized Meshing Add-on (OUR-OMA). It is based on a FEM approach for solving the displacement field at the crack tip based on the displacement field acquired by DIC, effectively dealing with noisy or partial data. However, this approach is believed to not be adequate for hierarchical thin-ply laminates as it requires an accurate FEM of the FPZ.

In this article, three J-integral formulations are compared and discussed to obtain the mode I translaminar toughness of hierarchical thin-plies from experimental displacement fields of CT specimens measured by DIC. The three proposed methods extend the initial algorithm proposed by Frossard [13] and Cugnoni et al. [15] by leveraging the ease of use of turnkey commercial stereo-DIC systems that have recently reached the market [50]. A piecewise cubic smoothing spline fitting of the displacement fields is implemented to filter the DIC noise while capturing the information without introducing significant bias. Indeed, the displacement fields are smooth, far enough from the FPZ. First, these three formulations' theoretical backgrounds and implementation details are presented. Then, a robustness and noise sensitivity study is conducted to validate the algorithm against synthetic data. Finally, the methods are applied to experimental data obtained from CT tests of cross-ply composite laminates. Application guidelines are established based on these results. They are intended as support documentation for the whole method, which is provided as a Python package [51] to diffuse the J-integral techniques further.

It should be noted that simultaneously with the publishing process of this paper, the German Aerospace Center (DLR) released a Python toolbox to perform fracture mechanics analysis from DIC and simulation results [52]. It contains, among other tools, a line J-integral implementation. In contrast to their approach, this study focuses solely on J-integral and further discusses its validity, robustness, and application to hierarchical thin-ply composites.

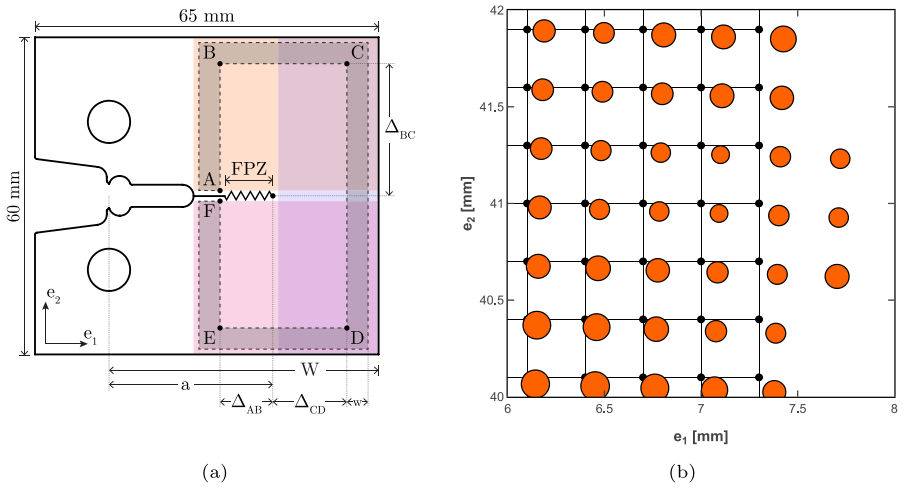

Fig. 2. (a) CT sample geometry and parametrization of the J-integral contours depicted as the shaded area between dashed lines and the upper, lower, and post crack fitting area shown rectangles filled with different colors; (b) illustration of the misalignment between the data points obtained from DIC and the regular grid in sample's referential over which the data are interpolated. The circle diameter scales with the normalized distance to the first neighbor. The rightmost points are outside of the convex hull defined by the remaining ones and are not interpolated.

2. J-integral implementation

This section introduces the theoretical background and the parameters required to derive the J-integral from a CT specimen whose displacement is monitored by DIC, regardless of the specific experimental setup. It also provides a rationale behind some details of the J-integral implementation as a Python script.

2.1. J-integral as a line integral formulation

The path-independent J-integral introduced independently by Cherepanov [43] and Rice [44] evaluates the potential energy change seen by an arbitrary enclosed region, assuming a homogeneous solid free of body forces and undergoing a 2D displacement field. When the enclosed region contains a crack, the J-integral may be used to quantify the potential energy accumulated before the crack propagation. It actually evaluates the energy required to propagate the crack, i.e., the material toughness.

The contour J-integral for a crack plane parallel to e_1 and perpendicular to e_2 (see Fig. 2(a)) is formulated as in Eq. (1), using the Einstein summation convention. Note that the crack length a is not required to derive the J-integral.

$$J = \int_{\Gamma} w de_2 - \int_{\Gamma} \sigma_{ij} n_j \frac{\partial u_i}{\partial e_1} ds \tag{1}$$

where:

i, j: planar cartesian indices

Γ: enclosing contour

w: strain density energy

σ: planar stress tensor

u: displacement field

n: outward unit normal vector along Γ

ds: infinitesimal arc length along Γ

Following Eq. (1), no other assumption than material homogeneity is made. However, constitutive laws should be assumed to derive the strain energy density and the stress tensor. Here the J-integral is evaluated at the surface of a composite laminate. Therefore orthotropic properties and plane stress conditions are assumed.

$$w = \begin{bmatrix} \varepsilon_{11} & \varepsilon_{22} & 2\varepsilon_{12} \end{bmatrix} C \begin{bmatrix} \varepsilon_{11} \\ \varepsilon_{22} \\ 2\varepsilon_{12} \end{bmatrix} \tag{2}$$

$$\begin{bmatrix} \sigma_{11} \\ \sigma_{22} \\ \sigma_{12} \end{bmatrix} = C \begin{bmatrix} \varepsilon_{11} \\ \varepsilon_{22} \\ 2\varepsilon_{12} \end{bmatrix} \tag{3}$$

$$C = \frac{1}{1-\nu_{12}\nu_{21}} \begin{bmatrix} E_1 & \nu_{21}E_1 & 0 \\ \nu_{12}E_2 & E_2 & 0 \\ 0 & 0 & G_{12}\left(1-\nu_{12}\nu_{21}\right) \end{bmatrix} \tag{4}$$

DIC software usually provides the strain field ε. It is, however, the result of calculations made on the grounds of assumptions not always explicit and perhaps not adequate for this peculiar application. Furthermore, should the displacement field not be perfect and subject to noise, proper pre-processing is required before computing the strain. Therefore, in this work, it is preferred to directly derive the strain field from the displacement field, which, under small strain assumption, gives:

$$\epsilon_{ij} = \frac{1}{2}\left(\frac{\partial u_i}{\partial e_j} + \frac{\partial u_j}{\partial e_i}\right) \tag{5}$$

While this formulation requires linearity over the evaluated contour Γ, the enclosed material may exhibit non-linearity, including, for instance, delamination or crack splitting. Since the J-integral is path independent, any arbitrary contour may be used. The J-integral is, therefore, convenient to characterize the toughness of composites that exhibit a complex FPZ, such as hierarchical thin-plies or thick-plies with extensive pull-out. In the proposed approach, a rectangular contour is used by convenience as depicted in Fig. 2(a). As the strain is formulated under the small displacement assumption, the contour is evaluated over undeformed coordinates. Thus, the path definition is not affected by the specimen rotation, and the initial material orientation is used when deriving the stress tensors. Importantly, different constitutive laws may be assumed according to the considered material as, for instance, a quasi-isotropic laminate.

2.2. J-integral as a simplified line integral formulation

Frossard [13] proposed a simplified J-integral formulation valid when the contour is defined at the edges of the sample, noticing that normal stresses at free edges are null. In this case, σ_{11} and σ_{22} are null over segment CD and segment BC or DE, respectively, as illustrated in Fig. 2(a).

2.3. J-integral as a surface integral formulation

As proposed by Li et al. [53], the divergence theorem can be applied to Eq. (1) to obtain a surface formulation as in Eq. (6). This formulation has been successfully implemented by Becker et al. [48]. Here, q is an arbitrary smooth function that translates the inner contour by the unit length along the crack direction (i.e., e_1) and vanishes on the outer contour. It may be interpreted as a virtual crack extension.

$$J = \int_A \left(\sigma_{ij}\frac{\partial u_i}{\partial e_1} - w\delta_{1j}\right)\frac{\partial q_1}{\partial x_j}\,dA \tag{6}$$

where:

i, j: planar cartesian indices

A: area defined by two enclosing contours

w: strain energy density

σ: planar stress tensor

u: displacement field

δ: Kronecker delta

q: smooth unit translation function

dA: infinitesimal surface

As shown in Eq. (1) to Eq. (6), only the elastic constant and the planar displacement field derivatives are required to apply the J-integral data reduction methods. The elastic constants are obtained from usual laminate characterization procedures or assumed from datasheets, while DIC is used to monitor the displacement fields at the sample surface. Implicitly, this approach assumes that the specimen surface displacements represent the homogenized material behavior. This assumption is reasonable as long the J-integral path does not include delaminated or damaged area. In practice, these conditions are met by using 90° outer plies to avoid the delamination of the surface ply when the crack propagates, and defining a path far enough from the FPZ. It is worth noting that for material prone to extensive delamination, such as thick-ply composites, the delaminated area should be carefully monitored. Looking for anomalies in the in-plane and out-of-plane displacement or strain fields may serve this purpose.

2.4. Displacement derivatives calculation

Due to the derivative evaluation, the J-integral approach is very sensitive to displacement noise [48]. To overcome this shortcoming, the displacement fields are fitted by a piecewise cubic smoothing spline as proposed by Frossard [13] and Cugnoni et al. [6]. It is achieved with the algorithm proposed by De Boor [54] and implemented in the CSAPS Python package [55]. As cubic, it is twice continuously differentiable and adequate to calculate derivatives. The natural property ensures that the second derivative is null at the endpoint though this feature is not required for this peculiar application. This algorithm was preferred to Scipy [56] spline fitting methods for computational performances and for the ease of controlling the approximation made through the smoothing factor. This latter is a parameter in the range [0,1], where 0 corresponds to the least-squares plane fit and 1 to the natural cubic spline interpolant. Note that the smoothing parameter is normalized to ensure repeatability between different datasets [55]. Finally, the displacement fields above the crack are fitted separately from those under the crack and those ahead of the crack to exclude the FPZ singularity as shown in Fig. 2(a).

The CSAPS algorithm interpolates and smooths splines over regular gridded data. In practice, the experimental displacement fields are usually not obtained over a suitable grid. For instance, Vic-3D outputs the results in the camera basis defined by the pixel matrix, which differs from the sample frame of reference as highlighted in Fig. 2(b). Moreover, once mapped over the sample frame of reference, the displacement field is not regular anymore. A pre-fitting operation is therefore required to interpolate the data over a regular grid. Here, it is achieved with the griddata method from Scipy package [56]. The grid step size is chosen to minimize the distance between the DIC points and the grid points. This approach effectively deals with missing data points as long they are inside the convex hull defined by the set of input points. Otherwise, the missing points are not extrapolated to avoid edge effects, and the grid size is reduced in order to be enclosed inside the convex hull.

2.5. Crack tip identification

As exposed in Sections 2.1 and 2.3, the crack length a is not involved in the J-integral derivation, and its measurement is not critical. The ERR is nonetheless traditionally reported in the literature as a function of the crack increment Δa. Moreover, the crack tip position was used to define the J-integral contour in the context of this study. As mentioned in Section 1, the crack tip definition is ambiguous in the presence of a large FPZ, especially if based on manual optical observation interpretation. Thus, a bias-free method is required to obtain an objective measure of the crack length. For instance, approaches based on the strain field or local rotational field around the crack tip have been successfully used in the literature [46]. Here, an effective crack length is defined based on the crack opening displacement (COD) profile extracted from the displacement fields. First, it is proposed that the upper and lower COD profile can be linearly fitted far enough from the crack tip and that their intersection is a point that moves with the crack tip but is usually located slightly farther. Thus, the position increment of this intersection can be seen as a good approximation of the crack length increment Δa between two frames. This approximation is later corrected as in Eq. (7) to account for the non-linearity of the COD near the crack tip. This correction scales the error committed on the crack length by the J_{Ic} value. In practice, the correction term is evaluated for the initial crack length a_0, which is known.

$$a_{intersec}^{corrected} = a_{intersec} - \left(a_{intersec}^{init} - a_0\right) \cdot \frac{\sqrt{J_{Ic,i}}}{\sqrt{J_{Ic}}} \tag{7}$$

The COD profile should be extracted as close as possible to the crack plane while avoiding the noise due to DIC edge effects and the zone affected by the crack tip. As a consequence, its extraction implementation is iterative. A more straightforward approach involves identifying the inflexion point introduced by the crack tip in a displacement profile evaluated parallel to the crack plane. The inflexion point position along e_1 is little affected by the position e_2 at which the displacement profile is evaluated and this method is therefore easier to implement. The displacement profile is extracted at an arbitrary distance e_2 from the crack plane and fitted with a piecewise cubic spline to evaluate its second derivative.

These methods address the crack tip identification in the propagation direction referred to as e_1 in this document. The identification in the e_2 direction is achieved by calculating the midpoint between the CT upper and lower arm center of rotation, which are identified by querying the minimal $\|u_1 u_2\|$ value. Note that the ERR may be reported more advantageously as a function of the crack opening displacement δ [31]. In this case, the COD is directly monitored with a clip gauge or by DIC measurement.

3. Numerical validation

3.1. Data generation

This section investigates the validation and robustness of the line, simplified, and surface J-integral previously formulated. Synthetic DIC data were generated using a compact tension test FEM implemented in Abaqus.[1] The analysis features a shell-element model of the 60 × 65 mm specimen used experimentally and whose geometry is reported in Fig. 2(a). A 2 mm symmetric controlled displacement was imposed at the loading holes through kinematic coupling. The singularity was introduced as quarter-point nodes

[1] The Python script used to generate the model is available along with the Python package for reproducibility purposes [51]. The figures presented in this paper were obtained with version v1.0.0-alpha.1.

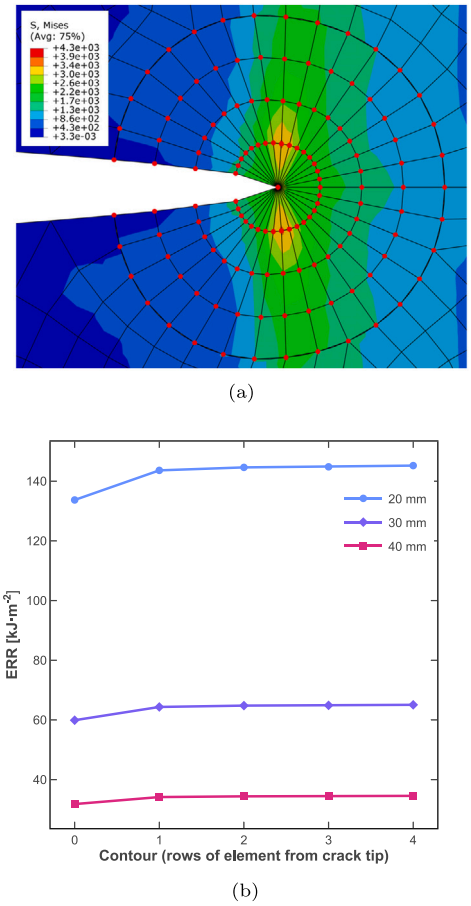

Fig. 3. (a) Details of the contours used to compute the FEM J-integral and (b) FEM J-integral results that converge quickly when moving away from the crack tip.

(collapsed elements with a node parameter of 0.25) with a single crack-tip node, see Fig. 3(a). The model was meshed with CPS8R elements using the free advancing front algorithm and a global size of 0.2 mm, resulting in an average distance to the first neighboring node of approximately 0.1 mm. The material properties were defined as an homogenized orthotropic cross-ply laminate, representative of an experimental specimen (see for instance Table 2). The displacement fields were extracted at each node, down-sampled with a 0.3 mm step size to account for the experimental results presented in this work, and fed to the J-integral algorithm, similarly to a DIC result. The 20, 30, and 40 mm crack lengths reported in Fig. 3(b) exhibit a FEM J-integral of 145.2, 65.1, and 34.6 kJ·m^{-2}, respectively. Note that these values correspond not to actual crack propagation but to the J_I values for a given applied displacement.

The displacement fields were additionally contaminated with additive white Gaussian noise to account for more realistic data. For this purpose, error values were drawn from a zero-mean normal distribution and added to each displacement component at each node. The distribution standard deviation was set to the standard deviation of the correlation errors reported in experimental DIC setups. Namely, 2.2e^{-4} mm and 1e^{-2} mm standard deviations were used. The former is valid for the experimental setup described in this work for which high-resolution cameras were used to monitor a regular CT specimen, while the latter is an extrapolation to sub-optimal conditions such as an OCT sample with standard resolution cameras.

Note that this noise generation suffers from a few shortcomings. First, the noise is generated for each individual component, whereas the confidence interval is reported as an overall magnitude. Thus, the generated noise is likely to be overestimated. Second, the noise is only applied to the displacement fields. Finally, this procedure does not account for the spatial distribution of the noise, which is likely with a DIC experimental setup, for instance when the lighting conditions are not truly uniform. Nevertheless, it provides valuable insights into the robustness of the J-integral algorithm.

3.2. Results

3.2.1. Crack tip identification

The intersection and inflexion procedures were applied to the synthetic data to identify the crack tip position as illustrated for the 30 mm crack length in Fig. 4(a), Fig. 4(b), and Fig. 4(d). Specifically, both u_2 and $\|u_1 u_2\|$ fields were used for the inflexion

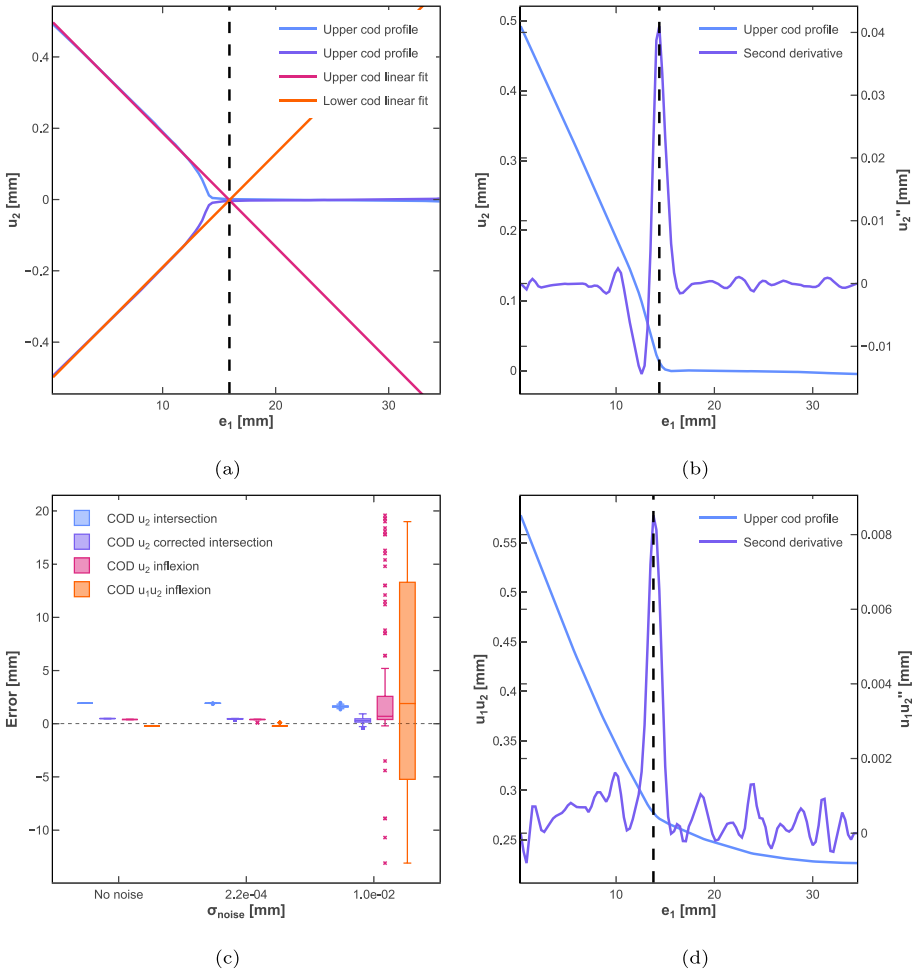

Fig. 4. (a), (b) and (d) Crack tip identification for the 30 mm crack length case using intersection method over u_2, inflexion method over u_2 and u_1u_2, respectively; (c) Distribution of the error made on the crack tip position for each method obtained with 100 Monte-Carlo draws, as a function of the artificial noise.

method. A Monte-Carlo method was used with 100 draws to account for the noise variability. The estimations reported in Fig. 4(c) were overall well-aligned with the true crack tip position. Under optimal conditions, i.e, no noise or $2.2e^{-4}$ mm standard deviation noise, the inflexion method error was bounded by the grid data step size. Here, this error was less than 0.3 mm. As expected, the intersection approach overestimated the crack tip position, here by approximately 2 mm. However, the error on the crack length was reduced to less than 0.5 mm after correction according to the initial offset and J_I influence (see Eq. (7)).

Under sub-optimal conditions, i.e, $1e^{-2}$ mm standard deviation noise, the inflexion methods predictions were heavily scattered over the whole range of data along e_1 direction. The high-level noise was the source of sharp local variations in the displacement field which led to the presence of the maximal second derivative at random locations. Thus, these methods still require further refinements, such as noise filtering, to be suitable when working with noisy data. On the other hand, the intersection method was very robust under sub-optimal conditions as the mean error remained below 0.5 mm with an interquartile range of 0.3 mm.

These findings result in recommending the inflexion methods as the best choice when ideal measurement conditions are feasible. Indeed, they provide a fast and direct estimation of the crack tip position and are convenient to implement. In comparison, the intersection method is implemented as a more complex iterative procedure that identifies the proper COD profiles and converges towards an intersection value. Furthermore, applying Eq. (7) to calculate the correction term and obtain an accurate crack tip position implies deriving the J-integral at least two times, the first time with a guess value to approximate the crack length and the second time to evaluate J_I with a contour adequately defined. However, the corrected intersection method is more robust and more suitable in practice, as shown in Section 4.

3.2.2. Data fitting

Data fitting is arguably a crucial step when applying the J-integral reduction methods. The choice of the smoothing value used by the CSAPS algorithm has a significant effect on the result as reported in Fig. 5. The error made on the J_I value, defined as

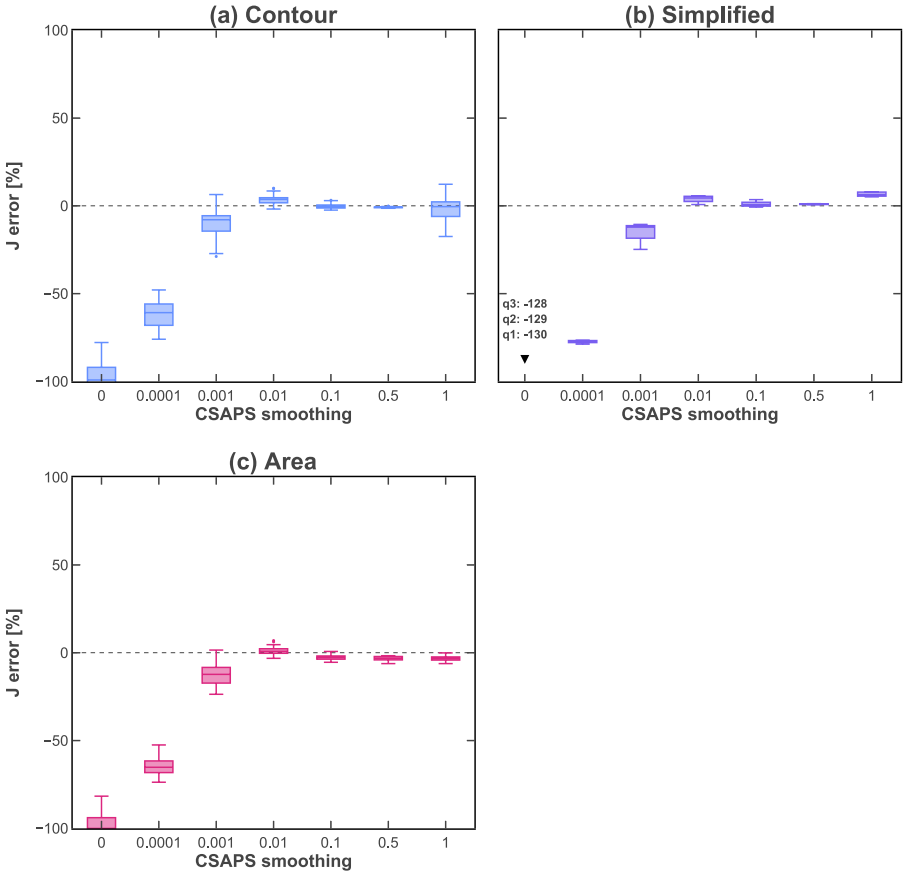

Fig. 5. Boxplots of the error committed on the J-integral results evaluated at a safe distance from the crack tip, as a function of the csaps smoothing value ranging from 0 to 1. Noise with $2.2e^{-4}$ mm standard deviation.

$error = \frac{J_{I,DIC} - J_{I,FEM}}{J_{I,FEM}}$ (here DIC refers to the synthetic DIC data), was represented as boxplots function of the smoothing value for $2.2e^{-4}$ mm noise. The remaining noise values produce similar results which are reported in the supplementary information (see Figs. A.18 and A.19).

Overall, the three J-integral algorithms provided an accurate J estimation with less than about 5% error for any smoothing value between $1e^{-2}$ and $5e^{-1}$. In detail, smoothing is beneficial in the presence of noise, even under optimal conditions. Indeed, a smoothing value of 1 corresponds to the natural cubic spline interpolant, which passes through each data point and fully captures both the noise and the rough nature of the discrete displacement field. Thus significant errors are made when evaluating field derivatives. However, the error increases when reducing the smoothing value too much (thus tending towards a linear interpolation). Qualitatively, a too-important smoothing effect fails to capture the local variations of the displacement fields, especially at the symmetry line of the CT specimens. On the other hand, the local variations are superseded by noise levels and smoothing is beneficial even if small field variations are lost (see Fig. A.19). Thus, a trade-off value of $1e^{-1}$ will be used. This value is only valid for this specific dataset. A convenient method to control that the smoothing value is adequate is to plot the fitting surface, as in Fig. 10(b), to evaluate overfitting or underfitting qualitatively. For a quantitative validation, a convergence study of the J-integral value as a function of the smoothing parameter should be performed as in Fig. A.19.

3.2.3. J-integral evaluation

A key property of the J-integral approach is path independence. Theoretically, J-integral evaluations over any contour enclosing the FPZ yield the same result. However, in practice, the results are affected for instance by edge effects, numerical singularities, and noise. Thus, a comprehensive numerical study of the path parametrization (see Fig. 2(a)) is proposed. The three J-integral methods were evaluated over all the successive contour from the crack tip to the sample edges by taking discrete values for offsets Δ_{AB}, Δ_{BC}, Δ_{CD}, Δ_{DE}, Δ_{EF} and surface width (for line and simplified algorithm, the width is always null, see Fig. 2(a)). The contours were kept symmetric with respect to the crack, thus Δ_{AB} is equal to Δ_{EF} and Δ_{BC} is equal to Δ_{DE}. This was done for the 30 mm crack length case as the crack tip is approximately at the middle of the crack propagation range.

Violin distributions [57] of the J-integral error as a function of these offsets are provided in the supplementary information. Under no noise or $2.2e^{-4}$ mm noise conditions, the three approaches performed similarly and provided distributions well centered

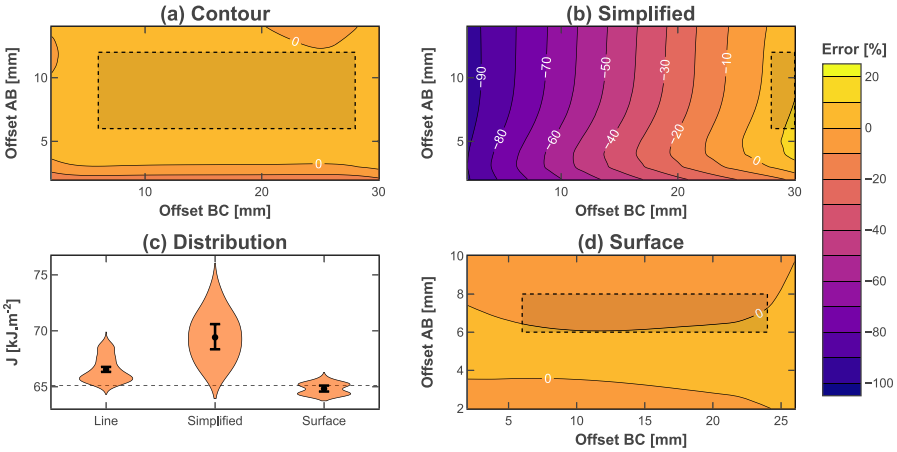

Fig. 6. Contours of the error incurred by the J-integral algorithm with respect to the FEM J-integral value, as a function of offsets Δ_{AB} and Δ_{BC} using (a) line, (b) simplified, and (d) surface methods, without noise. (c) Corresponding violin distributions obtained after constraining offsets Δ_{AB} and Δ_{BC} to the recommended range represented as a shaded black rectangle. The points stand for mean values and the error bars for the 99% confidence intervals obtained by bootstrapping over $1e^5$ iterations. The violin distributions are not normalized by the number of points for better readability.

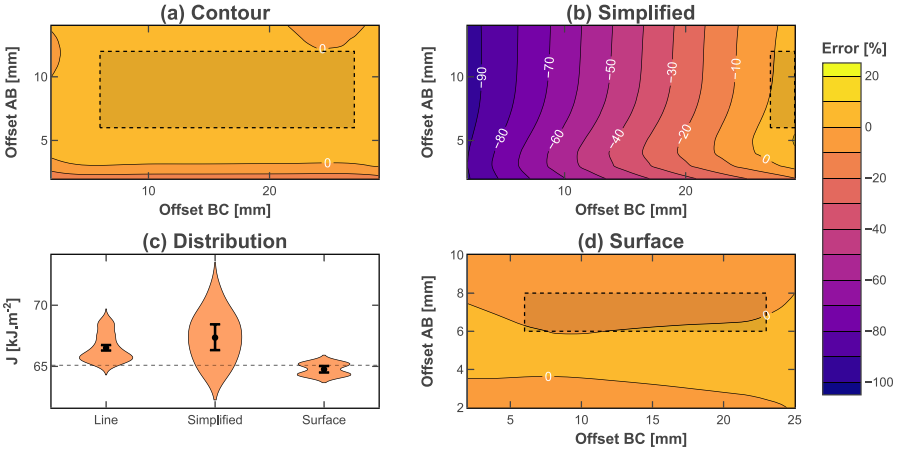

Fig. 7. Contours of the error incurred by the J-integral algorithm with respect to the FEM J-integral value, as a function of offsets Δ_{AB} and Δ_{BC} using (a) line, (b) simplified, and (d) surface methods, with a $2.2e^{-4}$ mm standard deviation noise. (c) Corresponding violin distributions obtained after constraining offsets Δ_{AB} and Δ_{BC} to the recommended range represented as a shaded black rectangle. The points stand for mean values and the error bars for the 99% confidence intervals obtained by bootstrapping over $1e^5$ iterations. The violin distributions are not normalized by the number of points for better readability.

around the true value for the majority of considered offsets (see Fig. A.20 to Fig. A.25). The only caveat was to avoid contour close to the crack tip, and to a lesser extent close to the sample edges, except for the simplified formulation that predicted correct results only when segments BC and DE are close to the sample edge. Here, 5 mm from the crack tip and 2 mm from the sample edges could be considered appropriate distances.

With high-level noise (see Fig. A.26 to Fig. A.28), the distributions were more scattered with aggravated edge effects but remained centered within a few percent of the FEM value. The surface algorithm was the most robust one. Increasing the width of the surface integral tended to reduce the scattering at the cost of slightly underestimating the FEM value. The distributions also highlighted that Δ_{CD} had minimal effect on the results and could safely be set to an arbitrary value.

The detailed effect of offsets Δ_{AB} and Δ_{BC} was then investigated while Δ_{CD} and surface width were both fixed to 6 mm. The J-integral error as a function of offset AB and offset BC is reported as contour maps for line, simplified, and surface algorithms under no noise, $2.2e^{-4}$ mm noise and $1e^{-2}$ mm noise (Fig. 6, Fig. 7 and Fig. 8, respectively). The maps clearly highlight the crack tip influence when offset Δ_{AB} was too close to the crack tip (close to 0 mm), as shown by the strong gradient of J-integral values. Interestingly, the offset BC value had almost no significant effect. An investigation of the J-integral terms reveals that the main contribution for segment BC was by far traction forces $-\sigma_{22}\frac{\partial u_2}{\partial e_1}de_1$. In this numerical study, the variation of displacement u_2 along e_1 direction was

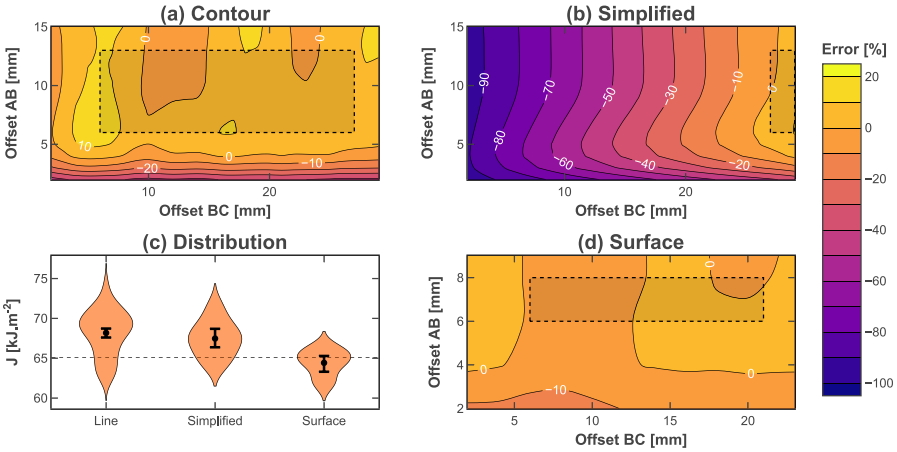

Fig. 8. Contours of the error incurred by the J-integral algorithm with respect to the FEM J-integral value, as a function of offsets Δ_{AB} and Δ_{BC} using (a) line, (b) simplified, and (d) surface methods, with a $1e^{-2}$ mm standard deviation noise. (c) Corresponding violin distributions obtained after constraining offsets Δ_{AB} and Δ_{BC} to the recommended range represented as a shaded black rectangle. The points stand for mean values and the error bars for the 99% confidence intervals obtained by bootstrapping over $1e^5$ iterations. The violin distributions are not normalized by the number of points for better readability.

little impacted by the crack tip. Thus, the position of segment BC was not significant. It also explains why Δ_{BC} value significantly affected the simplified formulation, as σ_{22} is only null at the sample edges. Note that the FEM did not account for the mechanisms such as fiber pull-out. Thus segment BC might require to be evaluated further from the crack tip in an experimental setup. Overall, the three methods were robust. They provided results within 10% error and path independence when contour offsets were set to appropriate values as depicted in Fig. 6 to Fig. 8 by shaded black rectangles. These results are aligned with the ones reported by Becker et al. [48] and Bergan et al. [31] when comparing the surface and the line J-integral with FEM results, respectively.

Under sub-optimal conditions, the noise was found to aggravate the crack tip detrimental influence, and J-integral results need to be evaluated further from it. The maps also reveal that the line J-integral suffered from oscillations when the noise was significant, without clear indications that would help identify the correct value (see Fig. 8). The oscillations seemed to follow a spatial pattern which may be related to the oscillations of the fitting splines. The surface algorithm was the most robust one. However, the surface width limited the number of possible contours. In contrast, the line method was evaluated over many more contours, leading to artificially thinner confidence intervals.

No correlation was found between the J-integral result and the cumulative nor the mean noise seen along the integration contour. It suggests that noise has an indirect effect on the J-integral, for instance, though derivative errors that would be affected both by the noise values and their spatial distribution.

As the simplified formulation yielded correct results only when segment BC was defined at the specimen edges, the same investigation was conducted with cropped data. Indeed, the displacement fields cannot be extracted at the edges with a DIC system and are, in practice, cropped. It is reported that cropping the data by 2 mm had little effect on the simplified value, with at most 2% difference. In this case, the most important source of error was the absence of data itself as the simplified J-integral validity decreased with the distance to the sample edge. Therefore, according to Figs. A.21, A.24c and A.27, the DIC data may be cropped up to approximately 5 mm while still providing results within 10% error.

3.3. Discussion

Using synthetic displacement fields generated by an Abaqus FEM, all three J-integral methods have been shown to be reliable, even if the data are severely affected by noise. To achieve these results, the J-integral should be evaluated far enough from the crack tip and use a suitable smoothing value. In this numerical study, offsets Δ_{AB} an Δ_{BC} of 5 mm and a smoothing value between $1e^{-2}$ and $5e^{-1}$ were found to be a sound choice. However, these values may be affected by experimental parameters like the FPZ size or the number of DIC points. They should therefore be checked for any given application. To do so, plotting the J-integral results as a surface response function of contour offset values is convenient for detecting steep gradients indicating the displacement field's local perturbations.

The FEM does not account for an FPZ but only for an idealized crack tip. However, the overall path independency of the J-integral indicates that it should remain valid if (i) the FPZ is encompassed by the J-integral path and (ii) the J-integral can be evaluated far enough from the FPZ. This could be verified numerically by further improving the FEM with, for instance, a cohesive law to account for an FPZ.

The simplified J-integral and the surface J-integral perform better than the line J-integral in the sense that they are less sensitive to noise under sub-optimal conditions. However, no physical criterion was identified to identify the correct J-integral values when the algorithms oscillate between multiple outputs. Sampling the results over a range of offsets far enough from the FPZ and the

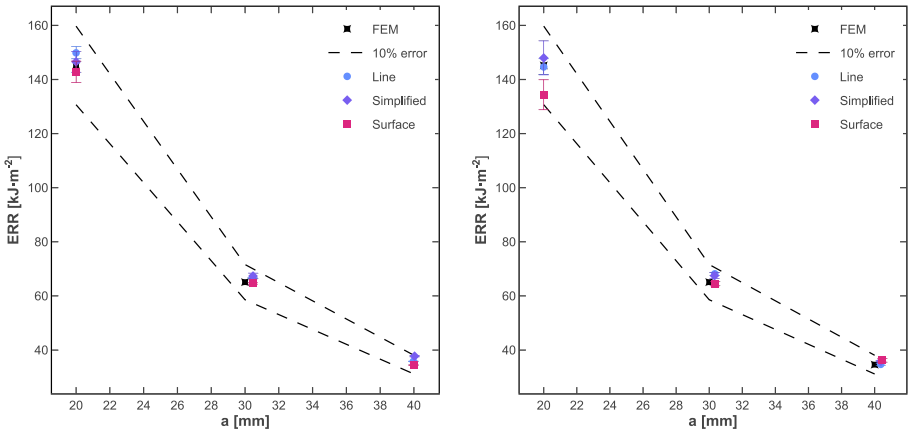

Fig. 9. J-integral results obtained for the 20, 30, and 40 mm crack-lengths implemented in Abaqus with (a) $2.2e^{-4}$ (b) and $1e^{-2}$ mm standard deviation noise. The crack tip position was estimated with the inflexion method for the former and the corrected interception method for the latter. Notice that with the corrected interception method, errors made on the J value for the initial crack length are propagated when estimating the crack length of the subsequent points.

sample edges addresses this issue, as the mean value was shown to be very well correlated with the FEM value. In this way, the line J-integral sensitivity to noise is compensated by the possibility of evaluating it over a great number of contours. On the other hand, the simplified formulation surface response exhibits very steep gradients. This means that the results can only be evaluated on a few points, which increases the risk of undetected errors.

Given these observations, it is proposed as good practice to systematically evaluate the J-integral over all available contour offset combinations and report the mean and the confidence interval. When using the simplified method, the segment BC should be evaluated as close as possible to the data edges (and thus the sample edges). In this study, an offset Δ_{BC} was found suitable from 2 mm before the maximal value to the maximal value. Using these guidelines, results were found to be in good agreement with the FEM values obtained for each crack length as depicted in Fig. 9. In the event that the three algorithms do not agree, the surface formulation can be considered the most robust. However, surface integration incurs by far the highest computational cost. As it is shown in Section 4, the line J-integral averaged over several contours provides very similar results and offers the best trade-off between toughness evaluation performances and computational cost.

4. Experimental validation

4.1. Experimental methods

This section discusses the application of the J-integral data reduction methods described in Section 2 and validated against synthetic data in Section 3 to an experimental dataset. CT specimens were tested following the same procedure described by Frossard [13]. Cracks were grown in four samples under monotonic displacement-controlled tests at a loading rate of 0.5 mm·min^{-1}. The stiffness of the loading chain was reported to be 20.8 kN·mm^{-1} [13], approximately 10 times greater than the stiffest reported specimen (2.1 kN·mm^{-1}, see Fig. 11(b)). This ratio ensures stable crack propagation.

CT specimens (60 × 65 mm) were produced by water-jet cutting according to the geometry reported in Fig. 2 from a 4.1 mm thick cross-ply laminate made by stacking 34–700 carbon fiber thin-ply prepregs provided by North ThinPly Technology. 90° plies were laid at the sample surface to avoid splitting. The 60 gsm plies were stacked three times, achieving an effective ply-block areal weight of 180 gsm. Such a thick-ply laminate typically exhibits extended pull-out and, thus, a large FPZ [12,13], making it suitable for validating the proposed methodology. Initial cracks were machined in the four samples using a diamond wire with a diameter of 0.125 mm to achieve an initial length a_0 ranging from 20.33 mm to 24.58 mm, as reported in Table 1. This resulted in a ratio $\frac{a_0}{W}$ (see Fig. 2(a)) of 0.39 and 0.48 respectively, which is similar to the one adopted by many authors [11–13,22,31,36]. Due to the laminate thinness (see Table 1), a numerical buckling study was performed to verify that the crack could propagate without risking buckling. This avoided the need for an anti-buckling device proposed by several authors [31,36].

The displacement fields were monitored using a commercial stereo-DIC setup provided by Correlated Solutions. Image correlation was performed with Vic-3D [58] version 8.6.3 software. Good practices recommended by Correlated Solutions and in the literature [59] were adopted, but no further DIC optimization was performed. Pictures were acquired by two 5Mpx Grasshopper3 GS3-U3-51S5M cameras equipped with Schneider Tele-Xenar 2.2 70 mm focal lenses, placed at approximately 800 mm from the specimen and with approximately 60 mm between the two cameras, defining a stereo-correlation angle of 4°. The system calibration was achieved with the maximal aperture, and the aperture was then reduced to increase the depth of field. The exposure time was set to 10 ms and the acquisition rate to 2 Hz. The former allows for a loading rate up to 2 mm·min^{-1} without pixel blurring. While the

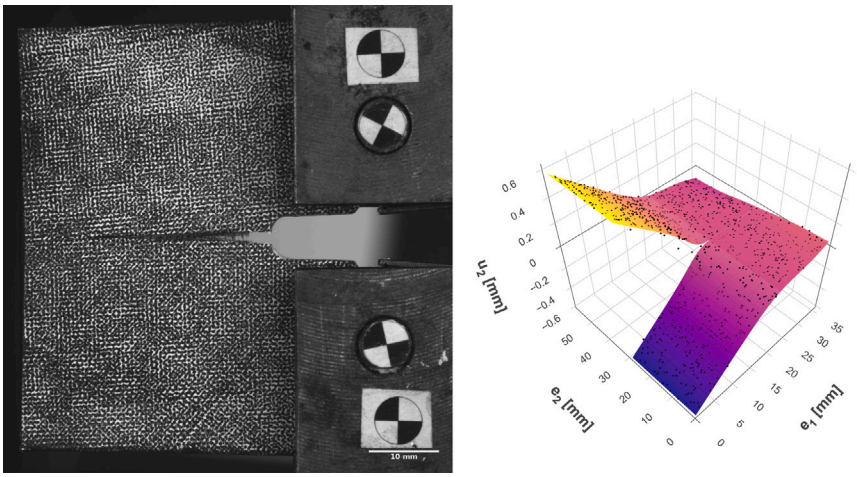

(a) (b)

Fig. 10. (a) Illustration of a typical CT specimen with its speckle obtained by rubber stamping; (b) Sample C experimental fitting surfaces obtained with a smoothing value of $1e^{-1}$.

Table 1
Sample properties.

Sample	Material	Stacking	W [mm]	a_0 [mm]	b [mm]	$\varnothing_a$ [μm]
A	34-700/TP415	$[90/0]_{ns}$	51	20.33	4.14±0.02	152
B				20.38	4.09±0.01	160
C				24.58	4.13±0.02	148
D				24.58	4.10±0.02	150

Table 2
Elastic constants obtained by classical laminated plate theory [60] assuming fiber datasheet values.

E_1 [GPa]	E_2 [GPa]	G_{12} [GPa]	ν_{12}
59.7	65.5	2.8	0.027

latter may seem slow compared to the crack propagation dynamics, the critical ERR is evaluated just before the crack propagation. Therefore, no more than 500 ms elapses between the crack propagation and the picture acquisition. Considering the loading rate of 0.5 mm·min^{-1}, the error made on the displacement at the pins is, at worst, $4.16e^{-3}$ mm. It represents $2.1e^{-1}$ % of the typical displacement at which the crack starts to propagate (see Fig. 11(a)).

A speckle was applied at the sample surface by spraying a thin layer of white matt acrylic paint followed by rubber stamping of black ink. An example is shown in Fig. 10(a). The rubber stamp from Correlated Solutions had a dot size of 0.18 mm and was applied several times with random orientations until more than 50% coverage was obtained (hence the obtained dots are roughly two times larger than the rubber stamp dot size). The DIC setup resulted in an average pixel size of about 33 μm. It corresponds to approximately 10 pixels per dot. Uniform lighting was obtained with two Nanlite LumiPad 25 panels.

A hybrid stereo calibration was performed within Vic-3D to reduce the uncertainty which was ultimately reported to be on average less or equal to $2.2e^{-4}$ mm and $3e^{-3}$ mm in and out of plane, respectively. An area of interest of approximately 35 × 60 mm was defined over the visible surface, excluding the loading fixtures but including the FPZ. The visible crack path for which correlation is not possible was then discarded based on the correlation error. A subset size of 47 pixels, suggested by Vic-3D, was used with Gaussian weights, optimized 8-tap, normalized squared difference, and exhaustive search. This resulted in a distance of approximately 0.3 mm between each data point, totaling about 20000 points. Finally, displacement fields were post-processed to remove rigid-body motions and project them over the sample coordinate system, then extracted and fed to the J-integral algorithms, along with the elastic constants reported in Table 2.

4.2. Results

In the following subsections, the detailed results are reported for sample C (a_0 = 24.5 mm). Similar findings were observed for the remaining samples. Sample C exhibited a typical CT load–displacement curve reported in Fig. 11(a). The load drops were used

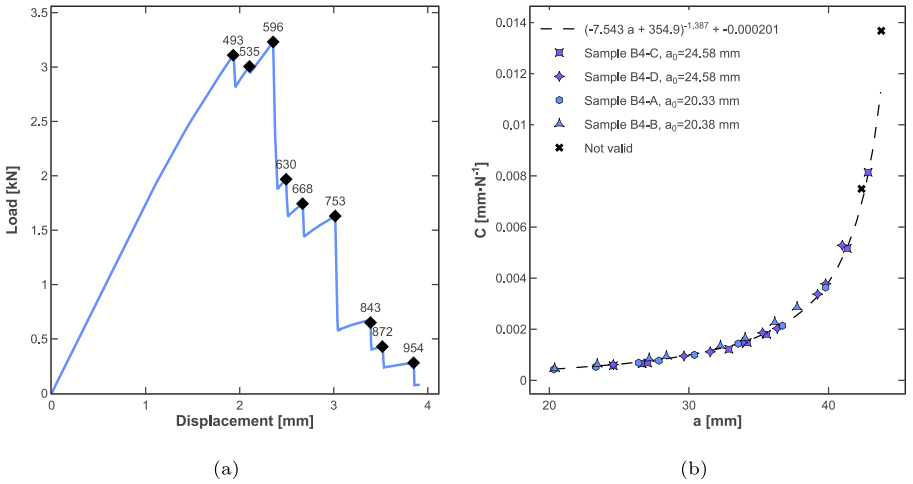

Fig. 11. (a) Typical load–displacement curve (sample C), a black marker indicates that a given point is used for the J-integral analysis and the corresponding DIC frame number is reported; (b) Compliance calibration.

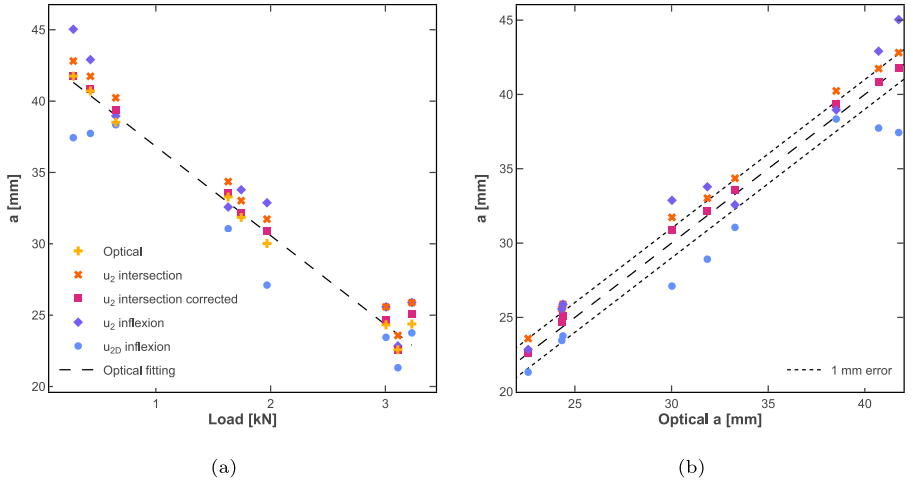

Fig. 12. (a) Crack length measured by different methods as a function of the applied load for sample C, and (b) comparison of these methods with respect to optical observations.

to identify the frames just before the crack propagation. Due to the frame acquisition rate, it was often required to rather analyze the previous frame, either because the crack was visually already propagated or the picture was blurred by the crack propagation dynamic. As previously discussed, this has little impact on the result.

4.2.1. Crack tip identification

The crack tip position estimations computed for each critical frame are shown as a function of the applied load in Fig. 12(a). The crack lengths obtained by optical observation of the crack surface are also reported. Overall, the load decreased with both the crack length and sample compliance increase, as expected [12]. On the other hand, the three first propagation points exhibited a different behavior where the load increased with the crack length (see Fig. 11(a)). This behavior, which was not observed for every sample, may be caused by an inappropriate initial crack tip radius. However, the crack propagation was reported to be notch independent as long the radius is less than 250 μm for cross-ply IM7/8552 CT specimens [22]. The apparent stiffness increase may thus be related to the development of the FPZ in association with an R-curve effect.

Regardless of this finding, the intersection and inflexion methods are in relatively good agreement with optical observation, as shown in Fig. 12(b), except when using $\|u_{2D}\|$ field. The latter was found to be more affected by sharp gradients when inspecting the second derivative. Especially, the corrected intersection method values were particularly close to the optical ones with less

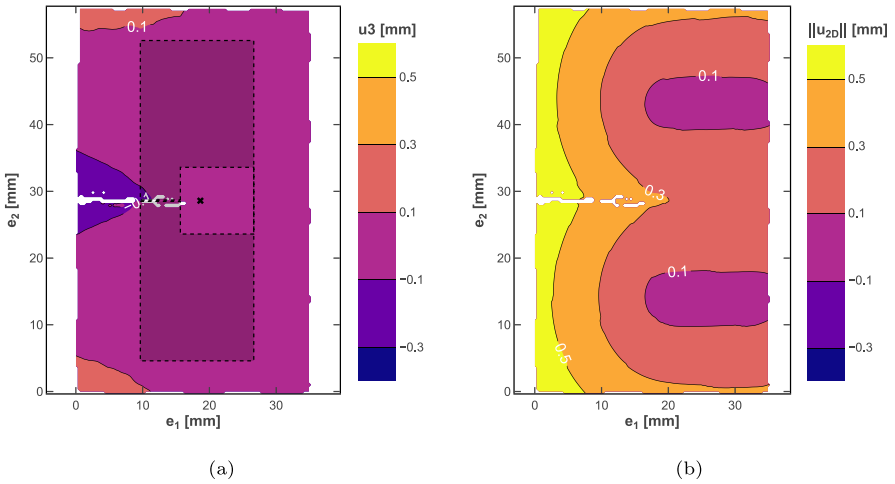

Fig. 13. (a) Out-of-plane displacement and (b) in-plane displacement norm monitored by DIC for frame 630 of sample C.

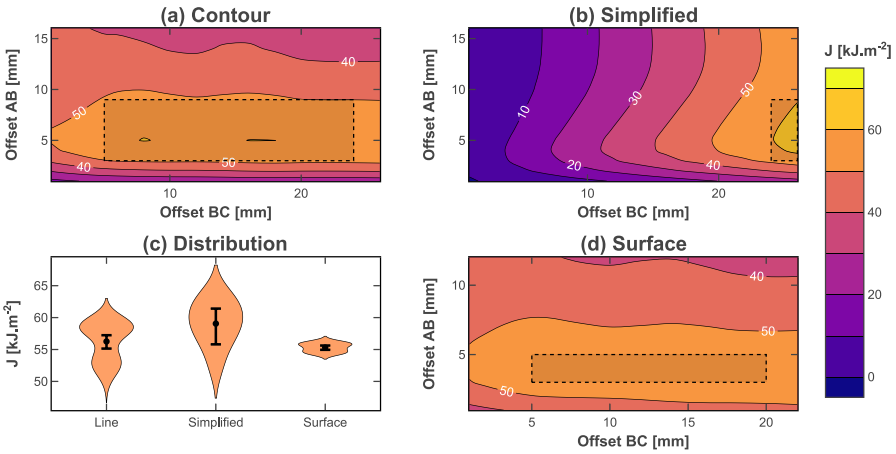

Fig. 14. Contours of the J-integral values for frame 630 of sample C as a function of offsets Δ_{AB} and Δ_{BC} using (a) line, (b) simplified and (b) surface methods. (c) Corresponding violin distributions obtained after constraining offsets Δ_{AB} and Δ_{BC} to the recommended range represented as a shaded black rectangle. The points stand for mean values and the error bars for the 99% confidence intervals obtained by bootstrapping over $1e^5$ iterations. The violin distributions are not normalized by the number of points for better readability.

than 1 mm difference. Thanks to the use of 90° plies at the sample surface, the crack front position at the sample surface could be identified without introducing too much bias. Thus, one may consider the corrected intersection method as a proper indicator of the surface crack position for this material. Furthermore, the COD profile taken far enough from the crack tip is the same at the sample surface and in the bulk material. Therefore, this method provides an estimation of the average crack front position, which is a better crack tip descriptor than the surface crack tip. X-ray computed tomography could be used to confirm this assumption as in [37]. Consequently, the corrected intersection method was used to estimate the crack tip position in the following results.

4.2.2. J-integral evaluation

A satisfying fitting of the experimental data was achieved with a smoothing value of $1e^{-1}$ (see Fig. 10(b)). As highlighted by Fig. 13(a), experimental samples may undergo a slight out-of-plane displacement. This out-of-plane displacement, which may reach up to 10% of the planar displacement (Fig. 13(b)) was not interpreted as buckling but rather as the consequence of slight fixtures misalignment. Indeed, they may induce torsion due to the thinness of the sample. As the out-of-plane displacements remained confined at the free corners of the sample, the test was considered to still be valid. However, J-integral results were severely affected if the evaluation contour, especially segment AB or EF encompassed an area with out-of-plane displacements. For instance, notice in Fig. 14(a) that there was a strong J_c gradient when Δ_{AB} spanned from 9 to 16 mm with respect to the crack tip. This range

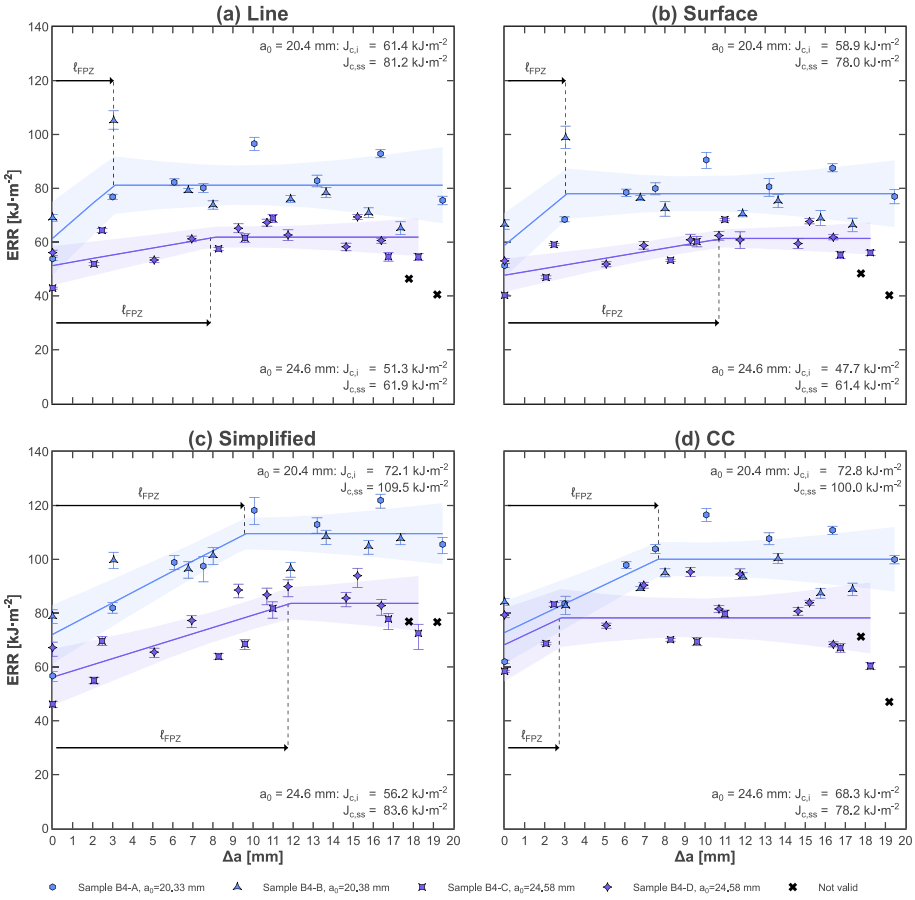

Fig. 15. Experimental ERR J_{Ic} for which a linear piecewise function has been fitted. The error bars stand for the confidence interval of each individual point while the bands stand for the confidence interval of the fitting, determined assuming a Student law.

corresponded specifically to the sample area undergoing out-of-plane displacements. Therefore, the guidelines expressed in Section 3 were supplemented to restrain, if possible, the J-integral evaluation to contours with less than 0.1 mm out-of-plane displacement, as represented by the shaded black rectangle in Fig. 13(a) and Fig. 14. Additional pathological cases have been observed and reported in the supplementary information (Fig. A.29 and Fig. A.30), the same approach of defining a contour that did not pass by the problematic area was applied.

Applying these guidelines to frame 630 of sample C, the line and surface J-integral methods yielded results in good agreement, slightly lower for the surface J-integral (see Fig. 14(c)). The surface J-integral formulation was the most robust one. The line J-integral produced more scattered results, but this was compensated by the fact that it could be evaluated over a broader range of offsets and averaged. Comparatively to these two methods, the simplified J-integral predicted roughly 5% larger results. These results were in good agreement with the numerical study (see Section 3). The same procedure was then carried out for each sample.

Additionally, a comparative compliance calibration (CC) was carried out as in [12]. The equation $C = \left(M_1 \cdot a + M_2\right)^{M_3} + C_0$ was fitted over the experimental compliance corrected by the setup compliance as reported in Fig. 11(b), as a function of the crack length a obtained by the corrected intersection method. The resulting ERR are presented in Fig. 15. They confirmed that the line and surface J-integral yield almost identical results for both initiation and steady-state J_{Ic}. As highlighted in the figure, the steady state ERR $J_{Ic,ss}$ seemed to be affected by the initial crack length. For instance, it was observed that according to the line J-integral, $J_{Ic,ss}$ increased by 31.2% from $a_0 = 24.6$ mm to $a_0 = 20.4$ mm. The initiation $J_{Ic,i}$ also increased by 19.7%, but too few experimental points are available to conclude.

It was also observed that both the simplified algorithm and CC accounted for the same behavior, but with an increase of respectively about 10% for the initiation value and about 30% for the steady state value compared to the line or surface J-integral.

Assuming that the FPZ is primarily the result of pull-out in the crack wake, an ERR plateau is reached when the FPZ grows to its maximum potential length. As such, plausible l_{FPZ} were reported in Fig. 15. Due to the limited number of points before the plateau, the true l_{FPZ} might be different, especially for the line and surface J-integral, which are affected by an outlier value at a Δa value of approximately 3 mm. Nevertheless, the FPZ size extrapolated from the J-integral R-curve is of the same order of magnitude as the observed size of the zone affected by pull-out in Fig. 16.

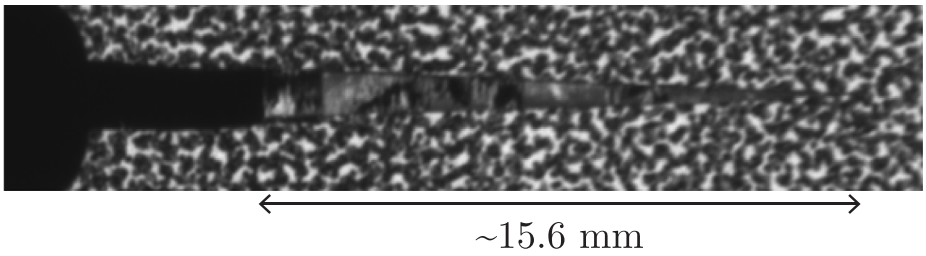

Fig. 16. Detailed view of fiber pull-out in the wake of the crack.

The toughness values reported in this work are for a cross-ply laminate. For the sake of completeness, it should be mentioned that the translaminar toughness of 0° plies can be calculated a posteriori applying the rule of mixtures defined by Eq. (8) [12,24,61], where t^{lam}, t^0 and t^{90} are the laminate thickness, the total thickness of 0°, and 90° plies, respectively. J_{Ic}^{90} corresponds to the intrinsic mode I intralaminar toughness of 90° plies. In M40JB-TP80ep samples, it was shown by Frossard to be one order of magnitude lower than the mode I translaminar toughness of 0° plies [13]. Neglecting it in Eq. (8) led to less than 2 % error. Following the same logic, the translaminar toughness obtained with the line J-integral is approximately 129 kJ·m^{-2} at initiation and 171 kJ·m^{-2} at propagation.

$$J_{Ic}^{0} = \frac{t^{lam} J_{Ic}^{lam} - t^{90} J_{Ic}^{90}}{t^{0}} \tag{8}$$

4.3. Discussion

Four CT specimens have been tested to characterize the translaminar toughness of a laminate that exhibits a large FPZ through extensive pull-out. The three J-integral methods have been successfully applied to derive the ERR. Among them, the line and surface yielded very close results and revealed an effect of the initial crack length a_0 on the steady-state ERR $J_{Ic,ss}$. Even if the few replicas call for caution, the contrast is significant and suggests that it is possible to reach a longer FPZ associated with a greater $J_{Ic,ss}$ when a_0 decreases. Therefore, the observed plateau can be interpreted as a virtual upper limit, corresponding to a stop in the development of the FPZ due to the sample size rather than as a true material property.

Interestingly, the experimental results obtained by compliance calibration were overestimated compared to the line or surface J-integral. Maimíet al. [33,39] previously reported the same contrast between R-curve and J-curve for high toughness samples. Then the same conclusion may be reached, that the compliance calibration tends to overestimate the ERR when the sample is too small compared to the FPZ size, but more data are required to confirm it. The compliance calibration relies on the LEFM theoretical frame, and while its validity is questionable when working with large FPZ, the compliance was obtained experimentally in this work and should capture the FPZ contribution.

On the other hand, the J-integral methods have been shown to be reliable in Section 3, and the displacement fields are of satisfactory quality. The elastic constant values used in this work could explain the contrast as they were derived by classical laminate theory. However, applying the same calculation to a quasi-isotropic laminate yielded a modulus of 43.9 GPa, in excellent agreement with the experimental value measured as 44.7±1.7 GPa. Following these arguments, the last possible cause is the crack length a measurement required to derive the compliance. The challenge of defining and measuring a, which increases as the FPZ gets larger, may very well explain the observed contrasts. Moreover, inaccurate measurement of a has a more significant impact on smaller samples as the change of compliance is proportionally more important for a given crack increment.

It is worth noting that the simplified J-integral values were found to be close to those calculated by compliance calibration, although no causal link has been established. The experimental results gathered in this investigation do not permit conclusions to be drawn about the most accurate J-integral method. However, the line and surface formulations provide similar results, although their formulation and implementation are significantly different. This observation indicates that they are more suitable than the simplified formulation. The latter adds the traction-free assumption, which overestimates the J-integral results compared to line and surface approaches, possibly due to edge effects, especially in an experimental setup where the sample edges are likely to undergo out-of-plane displacements. These considerations suggest that the displacement field perturbations or fitting errors close to the edge of the specimens are important factors that affect the J-integral calculation methods.

A FEM representative of the experiment, capturing the material toughness through cohesive elements, was implemented as detailed in [62] to provide perspective on these results. Note that the traction-separation laws were formulated to capture a $J_{Ic,i}$ and a $J_{Ic,ss}$ of approximately 60 kJ·m^{-2} and 80 kJ·m^{-2}, respectively. Simulation increments were analyzed with the line and simplified J-integral from the first load drop to simulate the discrete nature of the experimental crack propagation. In addition, the compliance calibration method was applied based on the crack lengths measured with the corrected intersection method. As shown in Fig. 17(a), the line J-integral and the compliance calibration correctly captured the laminate toughness. However, the simplified formulation

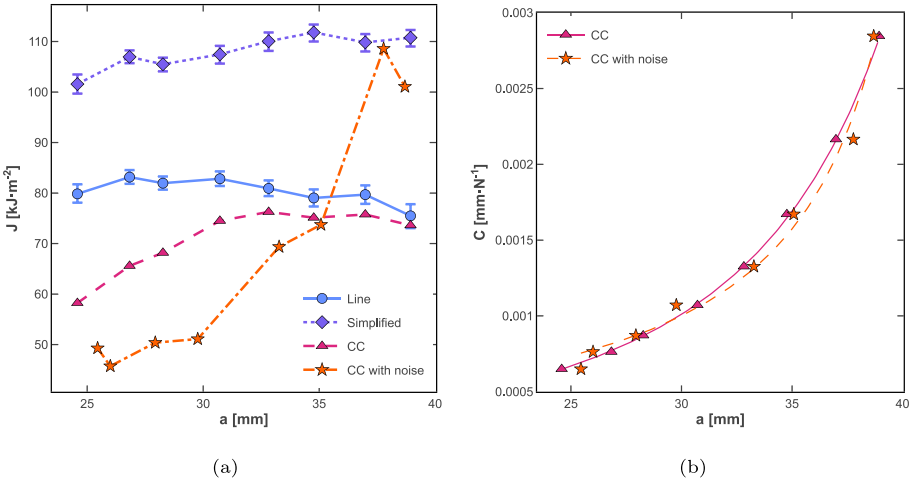

Fig. 17. (a) ERR J_{Ic} obtained by applying the J-integral and compliance calibration methods with the results of a FEM which captures the crack propagation with cohesive elements; (b) Corresponding compliance calibration. The error bars stand for the confidence interval of each individual point obtained with the J-integral approach.

significantly overestimated the values. Intriguingly, the J-integral did not capture the R-curve effect, contrasting with the reported experimental results. Moreover, the choice of the csaps smoothing value and the offset Δ_{BC} values significantly influenced the J-integral result. These three observations are possibly due to the presence of the cohesive elements along the crack path, which disrupt the displacement field, and should be investigated in future studies. Overall, they highlight that the proposed J-integral approach requires a convergence study of its parameters for each new application. Future works should investigate more systematic approaches to identify the adequate parameters. Furthermore, each method should be used within their respective recommended contour parameters, as defined in Section 3.3 and Section 4.2.2.

From Fig. 17(a), the compliance calibration may appear as more practical than the J-integral. However, its accuracy is the result of the excellent quality of the FEM data and the use of the corrected intersection method to measure the crack length, as highlighted by the fitting in Fig. 17(b). Lastly, if the crack length is perturbed with a random noise of $\pm$ 1 mm, the compliance calibration fails in capturing the material toughness (see Fig. 17(a)), although the compliance fitting is not strongly affected (see Fig. 17(b)). This confirms the interest of crack-length agnostic methods, such as the J-integral, over the compliance calibration.

Finally, as mentioned in Section 3, the computational cost of the surface J-integral is significant, by far the highest one. This cost is negligible when evaluating the J-integral value over one contour. However, the overhead becomes significant when evaluating several hundreds of contours per frame, as in this work. For instance, analyzing the nine frames of sample C on a workstation equipped with an AMD Ryzen 9 3900X processor required about 160 s for both line and simplified J-integral (which are evaluated simultaneously) while using the surface J-integral required roughly 1300 s. While the Python code could be optimized to address this issue, it demonstrates that the line and simplified formulations are more suitable for live data reduction of the translaminar toughness.

5. Conclusion

A set of three J-integral data reduction methods, namely line, simplified, and surface formulation, has been proposed to obtain the translaminar toughness of composites exhibiting large-scale FPZ. The methods were intended for CT specimens whose displacement fields are monitored by full-field DIC. From the proposed parametric study, the following concluding points are drawn:

- The three methods were shown to yield results in good agreement with FEM even under sub-optimal conditions (heavy noise).
- They were successfully applied to experimental data obtained from CT tests. A displacement field fitting along with a careful selection of the evaluation contour, far enough from the crack tip and out-of-plane displacement, ensured the resulting data reduction quality.
- Both the simplified formulation and the compliance calibration tend to overpredict the ERR. This was respectively attributed to edge effects and to the large FPZ, which makes the crack length measurement challenging.
- The three algorithms are provided as a Python package [51]. It may be associated with one of these DIC processors to obtain a full open-source pipeline [63–68].

CRediT authorship contribution statement

Guillaume Broggi: Writing – original draft, Visualization, Validation, Software, Methodology, Investigation, Formal analysis, Data curation, Conceptualization. **Joël Cugnoni:** Writing – review & editing, Supervision, Methodology, Funding acquisition, Formal analysis, Conceptualization. **Véronique Michaud:** Writing – review & editing, Supervision, Resources, Project administration, Funding acquisition.

Declaration of competing interest

The authors declare that they have no known competing financial interests or personal relationships that could have appeared to influence the work reported in this paper.

Data availability

Data is available on Zenodo, link provided in the manuscript [51].

Acknowledgments

The research leading to these results has been carried out within the framework of HyFiSyn project and has received funding from the European Union's Horizon 2020 research and innovation program under the Marie Skłodowska-Curie grant agreement No. 765881. The authors sincerely thank Prof. John Botsis for the project acquisition and the financial support of Guillaume Broggi, as well as for his scientific advice. Dr. Guillaume Frossard is gratefully thanked for sharing his initial algorithm. Dr. Frédéric Laurin is thanked for the discussion and suggestions on the J-integral perspectives. The technical support and advice of Raphaël Charvet and Robin Amacher were very much appreciated.

Appendix. Supplementary information

See Figs. A.18–A.30.

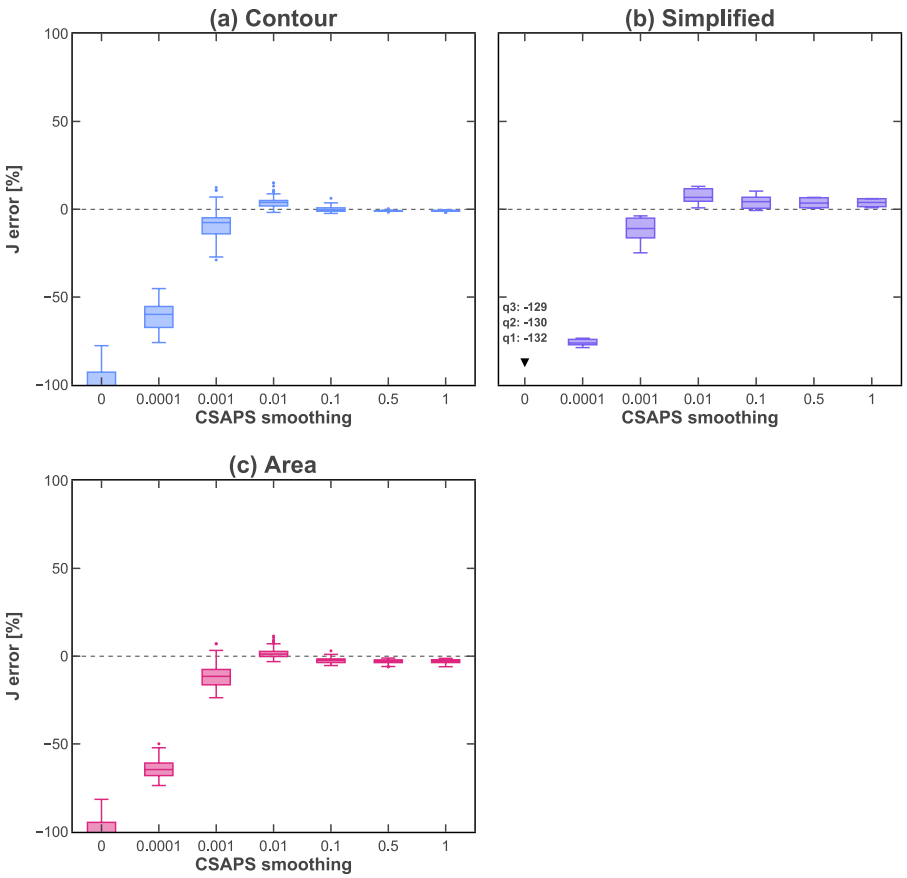

Fig. A.18. Boxplots of the error committed on the J-integral results evaluated at a safe distance from the crack tip, as a function of the csaps smoothing value ranging from 0 to 1. No noise.

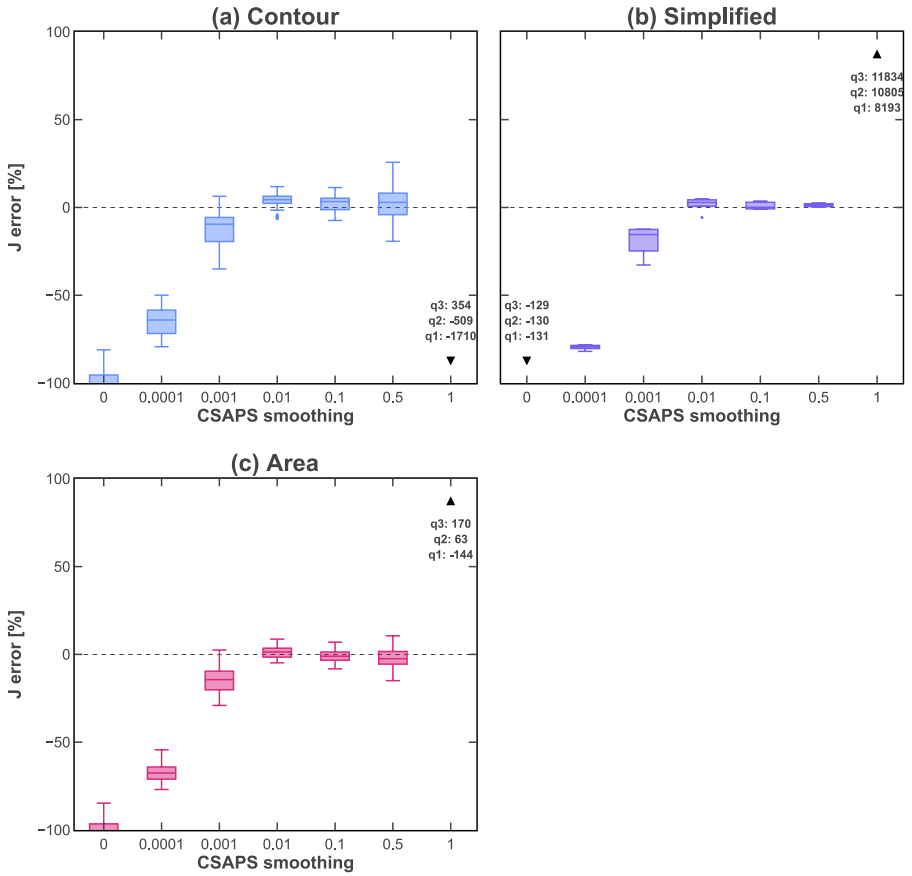

Fig. A.19. Boxplots of the error committed on the J-integral results evaluated at a safe distance from the crack tip, as a function of the csaps smoothing value ranging from 0 to 1. Noise with $1e^{-2}$ mm standard deviation.

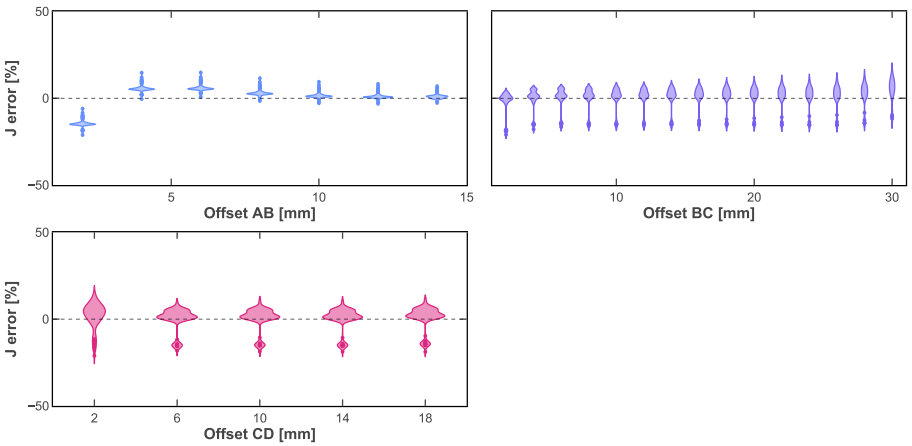

Fig. A.20. Violin distributions of the J-integral results obtained with the line formulation as a function of offset values ranging from the crack tip (0 mm) to the sample edge (maximal value). No noise. Only a subset of the offsets is reported for readability. The values close to the crack tip are significantly off and not reported. The FEM J-integral value is reported as a dashed line.

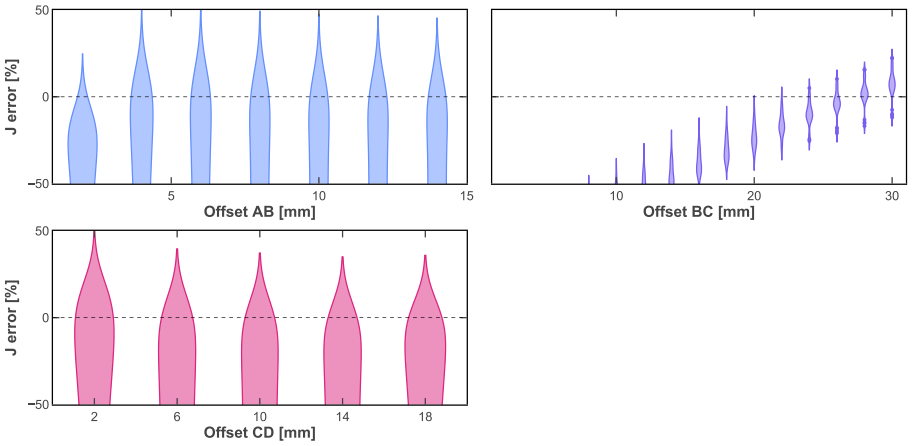

Fig. A.21. Violin distributions of the J-integral results obtained with the simplified formulation as a function of offset values ranging from the crack tip (0 mm) to the sample edge (maximal value). No noise. Only a subset of the offsets is reported for readability. The values close to the crack tip are significantly off and not reported. The FEM J-integral value is reported as a dashed line.

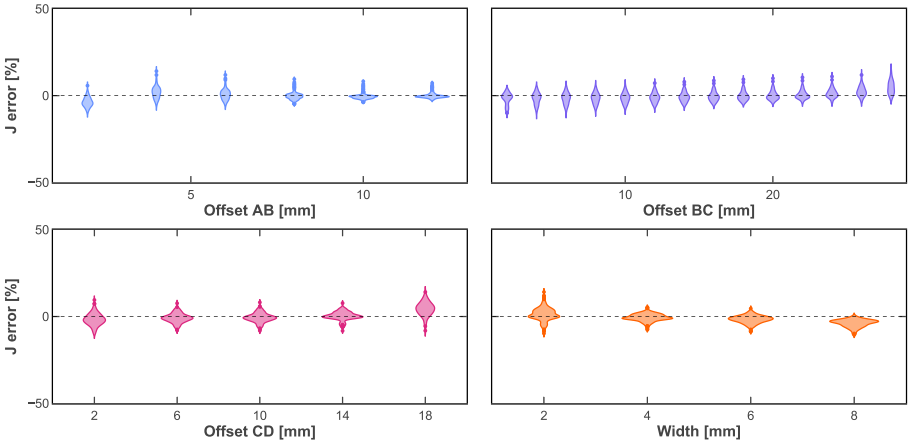

Fig. A.22. Violin distributions of the J-integral results obtained with the surface formulation as a function of offset values ranging from the crack tip (0 mm) to the sample edge (maximal value). No noise. Only a subset of the offsets is reported for readability. The values close to the crack tip are significantly off and not reported. The FEM J-integral value is reported as a dashed line.

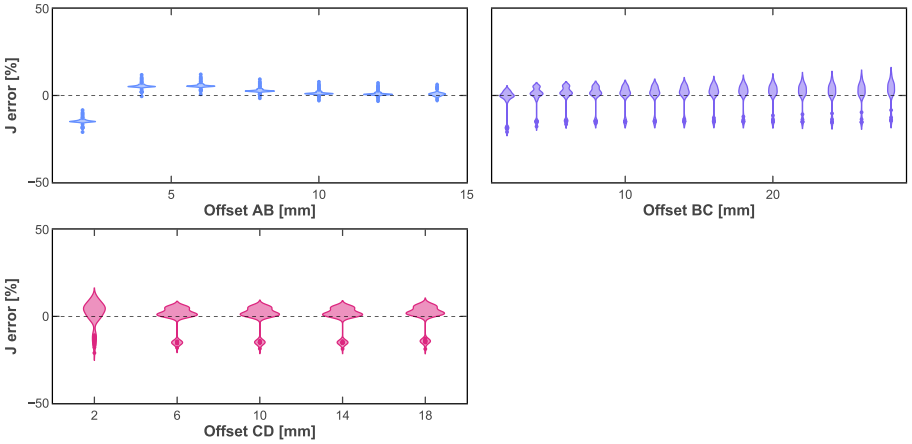

Fig. A.23. Violin distributions of the J-integral results obtained with the line formulation as a function of offset values ranging from the crack tip (0 mm) to the sample edge (maximal value). Noise with 2.2e−4 mm standard deviation. Only a subset of the offsets is reported for readability. The values close to the crack tip are significantly off and not reported. The FEM J-integral value is reported as a dashed line.

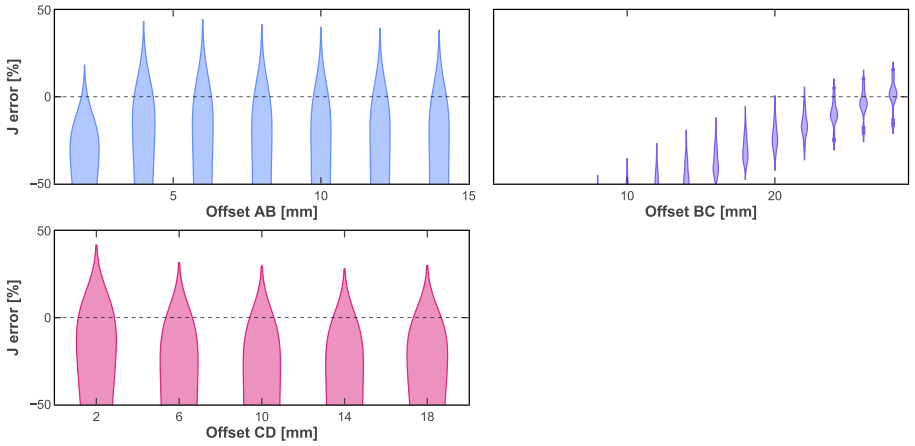

Fig. A.24. Violin distributions of the J-integral results obtained with the simplified formulation as a function of offset values ranging from the crack tip (0 mm) to the sample edge (maximal value). Noise with 2.2e−4 mm standard deviation. Only a subset of the offsets is reported for readability. The values close to the crack tip are significantly off and not reported. The FEM J-integral value is reported as a dashed line.

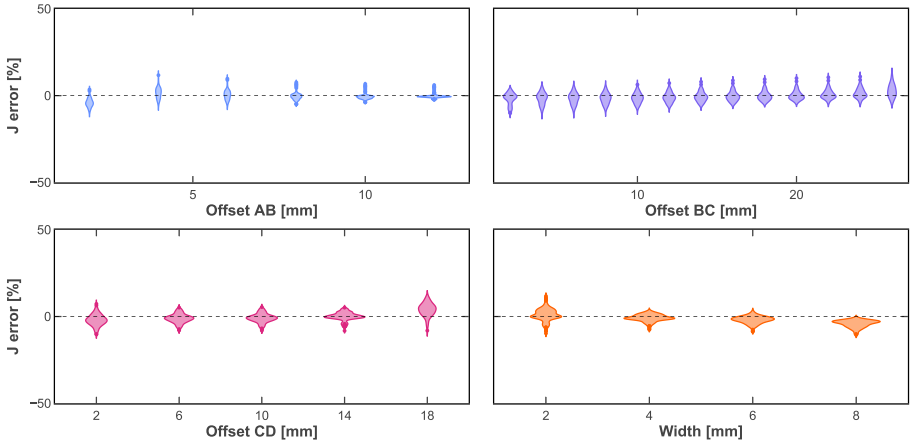

Fig. A.25. Violin distributions of the J-integral results obtained with the surface formulation as a function of offset values ranging from the crack tip (0 mm) to the sample edge (maximal value). Noise with 2.2e−4 mm standard deviation. Only a subset of the offsets is reported for readability. The values close to the crack tip are significantly off and not reported. The FEM J-integral value is reported as a dashed line.

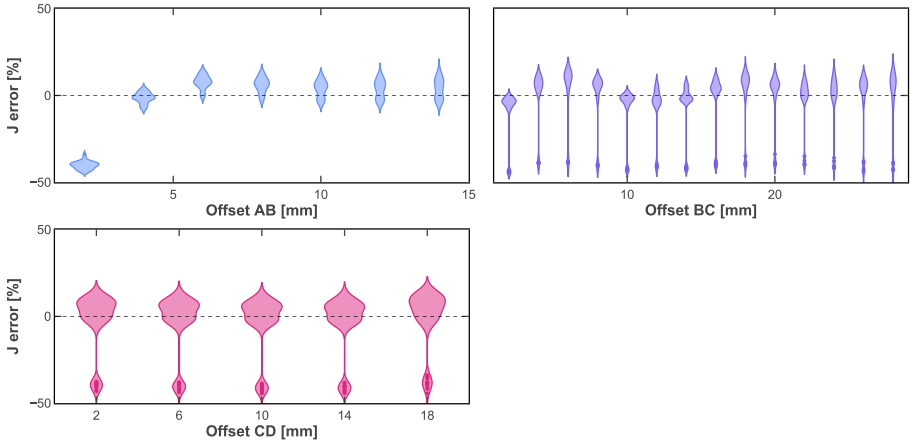

Fig. A.26. Violin distributions of the J-integral results obtained with the line formulation as a function of offset values ranging from the crack tip (0 mm) to the sample edge (maximal value). Noise with 1e−2 mm standard deviation. Only a subset of the offsets is reported for readability. The values close to the crack tip are significantly off and not reported. The FEM J-integral value is reported as a dashed line.

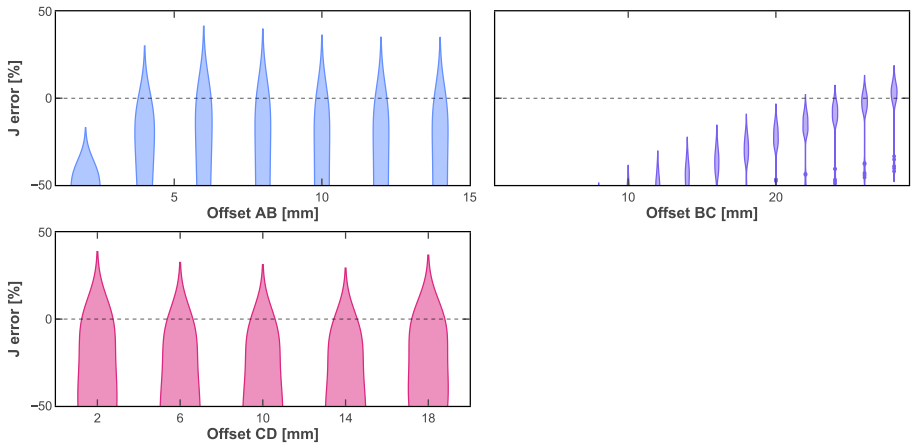

Fig. A.27. Violin distributions of the J-integral results obtained with the simplified formulation as a function of offset values ranging from the crack tip (0 mm) to the sample edge (maximal value). Noise with 1e-2 mm standard deviation. Only a subset of the offsets is reported for readability. The values close to the crack tip are significantly off and not reported. The FEM J-integral value is reported as a dashed line.

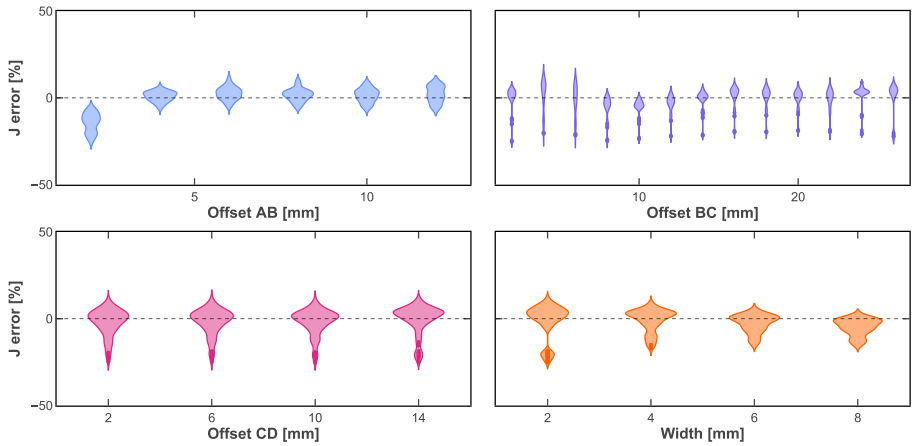

Fig. A.28. Violin distributions of the J-integral results obtained with the surface formulation as a function of offset values ranging from the crack tip (0 mm) to the sample edge (maximal value). Noise with 1e-2 mm standard deviation. Only a subset of the offsets is reported for readability. The values close to the crack tip are significantly off and not reported. The FEM J-integral value is reported as a dashed line.

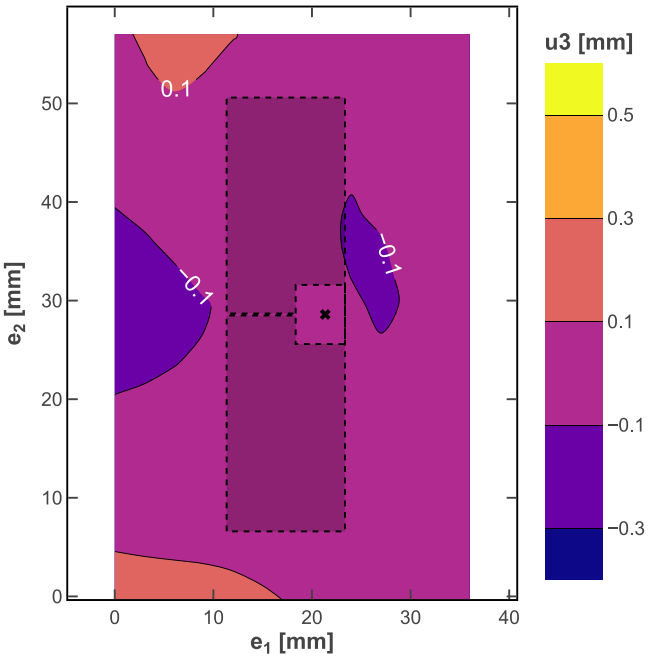

Fig. A.29. Out of plane displacement monitored by DIC for frame 753 of sample C.

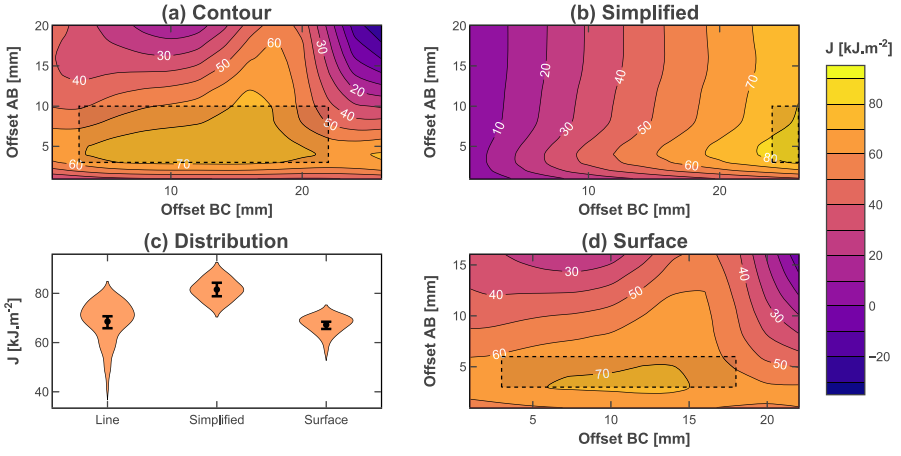

Fig. A.30. Contours of the J-integral values for frame 753 of sample C as a function of offsets Δ_{AB} and Δ_{BC} using (a) line, (b) simplified and (b) surface methods. (c) Corresponding violin distributions obtained after constraining offsets Δ_{AB} and Δ_{BC} to the recommended range represented as a shaded black rectangle. The points stand for mean values and the error bars for the 99% confidence intervals obtained by bootstrapping over $1e^5$ iterations. The violin distributions are not normalized by the number of points for better readability.

References

[1] Tavares SMO, de Castro PMST. An overview of fatigue in aircraft structures. Fatigue Fract Eng Mater Struct 2017;40(10):1510–29. http://dx.doi.org/10.1111/ffe.12631.

[2] Arteiro A, Furtado C, Catalanotti G, Linde P, Camanho PP. Thin-ply polymer composite materials: A review. Composites A 2020;132:105777. http://dx.doi.org/10.1016/j.compositesa.2020.105777.

[3] Sihn S, Kim R, Kawabe K, Tsai S. Experimental studies of thin-ply laminated composites. Compos Sci Technol 2007;67(6):996–1008. http://dx.doi.org/10.1016/j.compscitech.2006.06.008.

[4] Amacher R, Cugnoni J, Botsis J, Sorensen L, Smith W, Dransfeld C. Thin ply composites: Experimental characterization and modeling of size-effects. Compos Sci Technol 2014;101:121–32. http://dx.doi.org/10.1016/j.compscitech.2014.06.027.

[5] Saito H, Morita M, Kawabe K, Kanesaki M, Takeuchi H, Tanaka M, et al. Effect of ply-thickness on impact damage morphology in CFRP laminates. J Reinf Plast Compos 2011;30(13):1097–106. http://dx.doi.org/10.1177/0731684411416532.

[6] Cugnoni J, Amacher R, Kohler S, Brunner J, Kramer E, Dransfeld C, et al. Towards aerospace grade thin-ply composites: Effect of ply thickness, fibre, matrix and interlayer toughening on strength and damage tolerance. Compos Sci Technol 2018. http://dx.doi.org/10.1016/j.compscitech.2018.08.037.

[7] Camanho PP, Dávila CG, Pinho ST, Iannucci L, Robinson P. Prediction of in situ strengths and matrix cracking in composites under transverse tension and in-plane shear. In: CompTest 2004. Composites A 2006;37(2):165–76. http://dx.doi.org/10.1016/j.compositesa.2005.04.023.

[8] Catalanotti G. Prediction of in situ strengths in composites: Some considerations. Compos Struct 2019;207:889–93. http://dx.doi.org/10.1016/j.compstruct.2018.09.075.

[9] Kohler S, Cugnoni J, Amacher R, Botsis J. Transverse cracking in the bulk and at the free edge of thin-ply composites: Experiments and multiscale modelling. Composites A 2019;124:105468. http://dx.doi.org/10.1016/j.compositesa.2019.05.036.

[10] Wisnom M, Hallett S, Soutis C. Scaling effects in notched composites. J Compos Mater 2010;44(2):195–210. http://dx.doi.org/10.1177/0021998309339865.

[11] Laffan MJ, Pinho ST, Robinson P, Iannucci L. Measurement of the in situ ply fracture toughness associated with mode I fibre tensile failure in FRP. Part II: Size and lay-up effects. Compos Sci Technol 2010;70(4):614–21. http://dx.doi.org/10.1016/j.compscitech.2009.12.011.

[12] Teixeira R, Pinho S, Robinson P. Thickness-dependence of the translaminar fracture toughness: Experimental study using thin-ply composites. Composites A 2016;90:33–44. http://dx.doi.org/10.1016/j.compositesa.2016.05.031.

[13] Frossard G. Fracture of thin-ply composites: effects of ply thickness. 2017, p. 189. http://dx.doi.org/10.5075/epfl-thesis-8032.

[14] Ritchie RO. The conflicts between strength and toughness. Nature Mater 2011;10(11):817–22. http://dx.doi.org/10.1038/nmat3115.

[15] Cugnoni J, Frossard G, Amacher R, Botsis J. Translaminar fracture of regular and hybrid thin ply composites: Experimental characterization and modeling. 2018, p. 9.

[16] Bullegas G, Benoliel J, Fenelli PL, Pinho ST, Pimenta S. Towards quasi isotropic laminates with engineered fracture behaviour for industrial applications. Compos Sci Technol 2018;165:290–306. http://dx.doi.org/10.1016/j.compscitech.2018.07.004.

[17] Czél G, Rev T, Jalalvand M, Fotouhi M, Longana ML, Nixon-Pearson OJ, et al. Pseudo-ductility and reduced notch sensitivity in multi-directional all-carbon/epoxy thin-ply hybrid composites. Composites A 2018;104:151–64. http://dx.doi.org/10.1016/j.compositesa.2017.10.028.

[18] Mencattelli L, Pinho ST. Ultra-thin-ply CFRP Bouligand bio-inspired structures with enhanced load-bearing capacity, delayed catastrophic failure and high energy dissipation capability. Composites A 2020;129:105655. http://dx.doi.org/10.1016/j.compositesa.2019.105655.

[19] Danzi F, Tavares R, Xavier J, Fanteria D, Camanho P. Effects of hybridization and ply thickness on the strength and toughness of composite laminates. J Compos Mater 2021;55(30):4601–16. http://dx.doi.org/10.1177/00219983211041762.

[20] Plocher J, Mencattelli L, Narducci F, Pinho S. Learning from nature: Bio-inspiration for damage-tolerant high-performance fibre-reinforced composites. Compos Sci Technol 2021;208:108669. http://dx.doi.org/10.1016/j.compscitech.2021.108669.

[21] Anderson TL. Fracture mechanics: Fundamentals and applications. 4th ed. Boca Raton: CRC Press/Taylor & Francis; 2017.

[22] Laffan MJ, Pinho ST, Robinson P, McMillan AJ. Translaminar fracture toughness testing of composites: A review. Polym Test 2012;31(3):481–9. http://dx.doi.org/10.1016/j.polymertesting.2012.01.002.

[23] Catalanotti G, Arteiro A, Hayati M, Camanho PP. Determination of the mode I crack resistance curve of polymer composites using the size-effect law. Eng Fract Mech 2014;118:49–65. http://dx.doi.org/10.1016/j.engfracmech.2013.10.021.

[24] Laffan MJ, Pinho ST, Robinson P, Iannucci L. Measurement of the in situ ply fracture toughness associated with mode I fibre tensile failure in FRP. Part I: Data reduction. Compos Sci Technol 2010;70(4):606–13. http://dx.doi.org/10.1016/j.compscitech.2009.12.016.

[25] Pinho ST, Robinson P, Iannucci L. Fracture toughness of the tensile and compressive fibre failure modes in laminated composites. Compos Sci Technol 2006;66(13):2069–79. http://dx.doi.org/10.1016/j.compscitech.2005.12.023.

[26] Ortega A, Maimí P, González EV, Ripoll L. Compact tension specimen for orthotropic materials. Composites A 2014;63:85–93. http://dx.doi.org/10.1016/j.compositesa.2014.04.012.

[27] Dávila CG, Rose CA, Camanho PP. A procedure for superposing linear cohesive laws to represent multiple damage mechanisms in the fracture of composites. Int J Fract 2009;158(2):211–23. http://dx.doi.org/10.1007/s10704-009-9366-z.

[28] Sun C, Prewo K. The fracture toughness of boron aluminum composites. J Compos Mater 1977;11(2):164–75. http://dx.doi.org/10.1177/002199837701100204.

[29] Ahmadvashaghbash S, Mehdikhani M, Swolfs Y. Translaminar fracture of thin-ply composites: A Novel design for 4D synchrotron computed tomography. In: 20th European conference on composite materials. Lausanne, Switzerland; 2022, http://dx.doi.org/10.5075/epfl-298799_978-2-9701614-0-0.

[30] Sun X, Takeda S-i, Wisnom MR, Xu X. In situ characterization of trans-laminar fracture toughness using X-ray computed tomography. Compos Commun 2020;21:100408. http://dx.doi.org/10.1016/j.coco.2020.100408.

[31] Bergan A, Dávila C, Leone F, Awerbuch J, Tan T-M. A Mode I cohesive law characterization procedure for through-the-thickness crack propagation in composite laminates. Composites B 2016;94:338–49. http://dx.doi.org/10.1016/j.compositesb.2016.03.071.

[32] Ortega A, Maimí P, González EV, Trias D. Specimen geometry and specimen size dependence of the R-curve and the size effect law from a cohesive model point of view. Int J Fract 2017;205(2):239–54. http://dx.doi.org/10.1007/s10704-017-0195-1.

[33] Maimí P, Ortega A, González EV, Costa J. Should the translaminar fracture toughness of laminated composites be represented by the R or the J curve? A comparison of their consistency and predictive capability. Composites A 2022;156:106867. http://dx.doi.org/10.1016/j.compositesa.2022.106867.

[34] Kongshavn I, Poursartip A. Experimental investigation of a strain-softening approach to predicting failure in notched fibre-reinforced composite laminates. Compos Sci Technol 1999;59(1):29–40. http://dx.doi.org/10.1016/S0266-3538(98)00034-7.

[35] Li X, Hallett SR, Wisnom MR, Zobeiry N, Vaziri R, Poursartip A. Experimental study of damage propagation in Over-height Compact Tension tests. In: Special issue: CompTest 2008. Composites A 2009;40(12):1891–9. http://dx.doi.org/10.1016/j.compositesa.2009.08.017.

[36] Xu X, Wisnom MR, Mahadik Y, Hallett SR. Scaling of fracture response in Over-height Compact Tension tests. Composites A 2015;69:40–8. http://dx.doi.org/10.1016/j.compositesa.2014.11.002.

[37] Xu X, Sun X, Wisnom MR. Initial R-curves for trans-laminar fracture of quasi-isotropic carbon/epoxy laminates from specimens with increasing size. Compos Sci Technol 2021;216:109077. http://dx.doi.org/10.1016/j.compscitech.2021.109077.

[38] Catalanotti G, Camanho PP, Xavier J, Dávila CG, Marques AT. Measurement of resistance curves in the longitudinal failure of composites using digital image correlation. In: ICCM-17: Composites in biomedical applications, Compos Sci Technol In: ICCM-17: Composites in biomedical applications, 2010;70(13):1986–93.http://dx.doi.org/10.1016/j.compscitech.2010.07.022,

[39] Maimí P, Wagih A, Ortega A, Xavier J, Blanco N, Ponces Camanho P. On the experimental determination of the J-curve of quasi-brittle composite materials. Int J Fract 2020;224(2):199–215. http://dx.doi.org/10.1007/s10704-020-00456-0.

[40] Frossard G, Cugnoni J, Gmür T, Botsis J. An efficient method for fiber bridging traction identification based on the R-curve: Formulation and experimental validation. Compos Struct 2017;175:135–44. http://dx.doi.org/10.1016/j.compstruct.2017.04.032.

[41] Ortega A, Maimí P, González EV, Trias D. Characterization of the translaminar fracture Cohesive Law. In: CompTest 2015. Composites A 2016;91:501–9. http://dx.doi.org/10.1016/j.compositesa.2016.01.019.

[42] Ortega A, Maimí P, González EV, Sainz de Aja JR, de la Escalera FM, Cruz P. Translaminar fracture toughness of interply hybrid laminates under tensile and compressive loads. Compos Sci Technol 2017;143:1–12. http://dx.doi.org/10.1016/j.compscitech.2017.02.029.

[43] Cherepanov GP. Crack propagation in continuous media: PMM vol. 31, no. 3, 1967, pp. 476–488. J Appl Math Mech 1967;31(3):503–12. http://dx.doi.org/10.1016/0021-8928(67)90034-2.

[44] Rice JR. A path independent integral and the approximate analysis of strain concentration by notches and cracks. J Appl Mech 1968;35(2):379–86. http://dx.doi.org/10.1115/1.3601206.

[45] Herráez M, Pichler N, Pappas G, Blondeau C, Botsis J. Experiments and numerical modelling on angle-ply laminates under remote mode II loading. Composites A 2020;134:105886. http://dx.doi.org/10.1016/j.compositesa.2020.105886.
[46] Moutou Pitti R, Badulescu C, Grédiac M. Characterization of a cracked specimen with full-field measurements: Direct determination of the crack tip and energy release rate calculation. Int J Fract 2014;187(1):109–21. http://dx.doi.org/10.1007/s10704-013-9921-5.
[47] Montenegro DM, Canal LP, Botsis J, Zogg M, Studart AR, Wegener K. On the validity of the J-integral as a measure of the transverse intralaminar fracture energy of glass fiber-reinforced polyurethanes with nonlinear material behavior. Int J Solids Struct 2018;139–140:15–28. http://dx.doi.org/10.1016/j.ijsolstr.2018.01.019.
[48] Becker TH, Mostafavi M, Tait RB, Marrow TJ. An approach to calculate the J-integral by digital image correlation displacement field measurement. Fatigue Fract Eng Mater Struct 2012;35(10):971–84. http://dx.doi.org/10.1111/j.1460-2695.2012.01685.x.
[49] Barhli S, Mostafavi M, Cinar A, Hollis D, Marrow T. J-integral calculation by finite element processing of measured full-field surface displacements. Exp Mech 2017;57(6):997–1009. http://dx.doi.org/10.1007/s11340-017-0275-1.
[50] Pan B. Digital image correlation for surface deformation measurement: Historical developments, recent advances and future goals. Meas Sci Technol 2018;29(8):082001. http://dx.doi.org/10.1088/1361-6501/aac55b.
[51] Broggi G, Cugnoni J, Michaud V. A Python implementation of J-integral data reduction methods for composite toughness. 2022, http://dx.doi.org/10.5281/zenodo.7307418.
[52] Strohmann T, Melching D, Florian P, Klein A, Eric D, Requena G, et al. Crack analysis tool in Python - CrackPy. 2022, http://dx.doi.org/10.5281/ZENODO.7319652.
[53] Li FZ, Shih CF, Needleman A. A comparison of methods for calculating energy release rates. Eng Fract Mech 1985;21(2):405–21. http://dx.doi.org/10.1016/0013-7944(85)90029-3.
[54] De Boor C. A practical guide to splines: With 32 figures. Applied mathematical sciences, no. v. 27, Rev. ed. New York: Springer; 2001.
[55] Prilepin E. Csaps: Cubic spline approximation (smoothing).
[56] Virtanen P, Gommers R, Oliphant TE, Haberland M, Reddy T, Cournapeau D, Burovski E, Peterson P, Weckesser W, Bright J, van der Walt SJ, Brett M, Wilson J, Millman KJ, Mayorov N, Nelson ARJ, Jones E, Kern R, Larson E, Carey CJ, Polat İ, Feng Y, Moore EW, VanderPlas J, Laxalde D, Perktold J, Cimrman R, Henriksen I, Quintero EA, Harris CR, Archibald AM, Ribeiro AH, Pedregosa F, van Mulbregt P, SciPy 10 Contributors, Vijaykumar A, Bardelli AP, Rothberg A, Hilboll A, Kloeckner A, Scopatz A, Lee A, Rokem A, Woods CN, Fulton C, Masson C, Häggström C, Fitzgerald C, Nicholson DA, Hagen DR, Pasechnik DV, Olivetti E, Martin E, Wieser E, Silva F, Lenders F, Wilhelm F, Young G, Price GA, Ingold G-L, Allen GE, Lee GR, Audren H, Probst I, Dietrich JP, Silterra J, Webber JT, Slavič J, Nothman J, Buchner J, Kulick J, Schönberger JL, de Miranda Cardoso JV, Reimer J, Harrington J, Rodríguez JLC, Nunez-Iglesias J, Kuczynski J, Tritz K, Thoma M, Newville M, Kümmerer M, Bolingbroke M, Tartre M, Pak M, Smith NJ, Nowaczyk N, Shebanov N, Pavlyk O, Brodtkorb PA, Lee P, McGibbon RT, Feldbauer R, Lewis S, Tygier S, Sievert S, Vigna S, Peterson S, More S, Pudlik T, Oshima T, Pingel TJ, Robitaille TP, Spura T, Jones TR, Cera T, Leslie T, Zito T, Krauss T, Upadhyay U, Halchenko YO, Vázquez-Baeza Y. SciPy 1.0: Fundamental algorithms for scientific computing in Python. Nature Methods 2020;17(3):261–72. http://dx.doi.org/10.1038/s41592-019-0686-2.
[57] Hintze JL, Nelson RD. Violin plots: A box plot-density trace synergism. Amer Statist 1998;52(2):181–4. http://dx.doi.org/10.2307/2685478.
[58] McGowan D, Ambur D, McNeill S. Full-field structural response of composite structures: analysis and experiment. In: 44th AIAA/ASME/ASCE/AHS/ASC structures, structural dynamics, and materials conference. Norfolk, Virginia: American Institute of Aeronautics and Astronautics; 2003, http://dx.doi.org/10.2514/6.2003-1623.
[59] International Digital Image Correlation Society Jones E, Iadicola M, Bigger R, Blaysat B, Boo C, Grewer M, et al. A good practices guide for digital image correlation. Tech. rep., 1st ed. International Digital Image Correlation Society; 2018, http://dx.doi.org/10.32720/idics/gpg.ed1.
[60] Hauffe A. eLamX^2 - Expandable laminate explorer. 2022.
[61] Camanho PP, Catalanotti G. On the relation between the mode I fracture toughness of a composite laminate and that of a 0° ply: Analytical model and experimental validation. Eng Fract Mech 2011;78(13):2535–46. http://dx.doi.org/10.1016/j.engfracmech.2011.06.013.
[62] Broggi G. Multi-scale characterization and modeling of notched strength and translaminar fracture in hybrid thin-ply composites based on different carbon fiber grades. Ph.D. thesis, EPFL, Lausanne, Switzerland; 2023.
[63] Turner DZ. Digital image correlation engine (DICe) reference manual. Sandia Report SAND2015-10606 O, 2015.
[64] Solav D, Moerman KM, Jaeger AM, Genovese K, Herr HM. MultiDIC: An open-source toolbox for multi-view 3d digital image correlation. IEEE Access 2018;6:30520–35. http://dx.doi.org/10.1109/ACCESS.2018.2843725.
[65] Belloni V, Ravanelli R, Nascetti A, Di Rita M, Mattei D, Crespi M. py2DIC: A new free and open source software for displacement and strain measurements in the field of experimental mechanics. Sensors 2019;19(18):3832. http://dx.doi.org/10.3390/s19183832.
[66] Olufsen SN, Andersen ME, Fagerholt E. μDIC: An open-source toolkit for digital image correlation. SoftwareX 2020;11:100391. http://dx.doi.org/10.1016/j.softx.2019.100391.
[67] Das PP, Elenchezhian MRP, Vadlamudi V, Reifsnider K, Raihan R. RealPi2dDIC: A low-cost and open-source approach to in situ 2D Digital Image Correlation (DIC) applications. SoftwareX 2021;13:100645. http://dx.doi.org/10.1016/j.softx.2020.100645.
[68] Damien André / Pydic · GitLab, GitLab, https://gitlab.com/damien.andre/pydic.